

Logarithmic Mathematical Morphology: theory and applications

Guillaume Noyel,

Abstract

Classically, in Mathematical Morphology, an image (i.e., a grey-level function) is analysed by another image which is named the structuring element or the structuring function. This structuring function is moved over the image domain and summed to the image. However, in an image presenting lighting variations, the analysis by a structuring function should require that its amplitude varies according to the image intensity. Such a property is not verified in Mathematical Morphology for grey level functions, when the structuring function is summed to the image with the usual additive law. In order to address this issue, a new framework is defined with an additive law for which the amplitude of the structuring function varies according to the image amplitude. This additive law is chosen within the Logarithmic Image Processing framework and models the lighting variations with a physical cause such as a change of light intensity or a change of camera exposure-time. The new framework is named Logarithmic Mathematical Morphology (LMM) and allows the definition of operators which are robust to such lighting variations. In images with uniform lighting variations, those new LMM operators perform better than usual morphological operators. In eye-fundus images with non-uniform lighting variations, a LMM method for vessel segmentation is compared to three state-of-the-art approaches. Results show that the LMM approach has a better robustness to such variations than the three others.

Index Terms

Mathematical morphology, lighting variations, order-statistic filters, intensity-variant structuring function, robustness to lighting variations, Asplund metric.



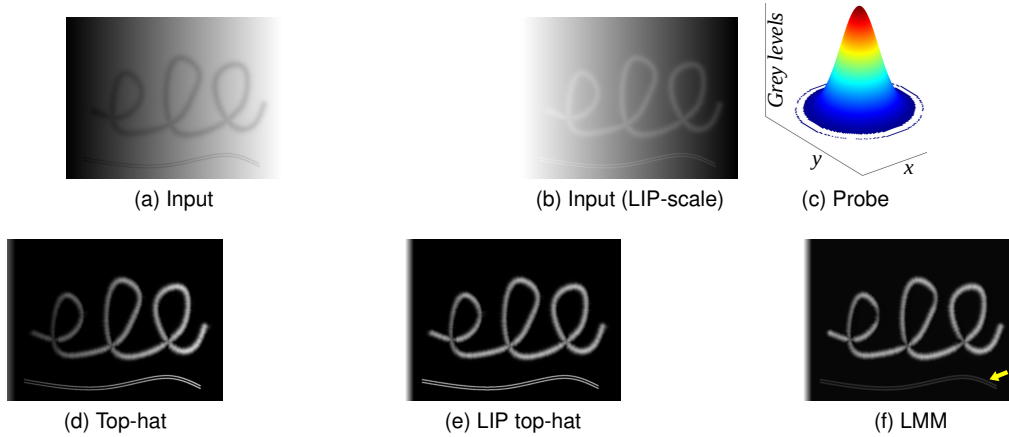


Fig. 1. Comparison between usual methods and LMM to detect a spiral in (a) a simulated image also containing confounders : two close curves and a lighting drift. (b) This image is converted in LIP-greyscale (i.e. the inverted greyscale). (d) The top-hat with a flat disk extracts the spiral and both curves. However, it is sensitive to the lighting drift. (e) The LIP-top-hat with a flat disk extracts the spiral and both curves without the lighting drift. (f) The LMM operator is a LIP-difference between two LIP-openings: the first LIP-opening is done by (c) a probe composed of a ring and a Gaussian and the second by a probe composed of the same ring. The LMM operator successfully extracts the spiral and strongly attenuates both close curves.

Logarithmic Mathematical Morphology: theory and applications

1 INTRODUCTION

MATHEMATICAL Morphology (MM) was originally defined by Matheron [1] for sets and then extended to functions with real values by Serra [2], Sternberg [3], [4] and Maragos [5]. In this latter case, a function is analysed by another function named structuring element or structuring function. This extension includes grey level images whose values are within the bounded interval $[0, M[$ of the real space \mathbb{R} . For example, for 8 bit-digitised images, M is equal to 256. Generally, structuring functions and morphological operators are invariant under horizontal translations (i.e. in space) and under vertical translations (i.e. in intensity) [6].

However, the application of MM to grey level images presents two limitations. (1) Firstly, albeit grey level images have bounded values, MM was defined for functions with values within the unbounded real space \mathbb{R} [7], [8]. Indeed, given an image f and a structuring function b both defined on the same domain $D \subset \mathbb{R}^n$ and whose values are within the range $[0, M[$, their sum $f + b$ does not lie within the interval $[0, M[$. Practical solutions to this issue consist of using either (i) a structuring function whose supremum is equal to zero, (ii) or a flat structuring element whose values are equal to zero (iii) or to truncate the values of the resulting image to the maximal possible value, M [7]. (2) Secondly, adding a structuring function to an image without taking into account the image intensity into the amplitude of the structuring function is not physically justified. As in human vision, the eye response to light intensity variations is known to be logarithmic [9], [10], [11], [12], [13], it follows that in images the contrast variations are also logarithmic and the darkest variations are more attenuated than the brightest ones [14], [15]. The amplitude of the structuring function must therefore depend on the image intensity, i.e. the grey value. Such a structuring function will be invariant under horizontal translation but not under vertical translation, i.e. in the intensity domain $[0, M[$.

In parallel to the genesis of grey-level MM, Jourlin has developed the Logarithmic Image Processing (LIP) model which is adapted to human vision [9], [16], [17] and which allows to process images as a human eye would do. It is not only rigorously defined from a mathematical point of view, but it also possesses strong physical properties. In particular, the LIP-addition \triangle of two images results in an image (with bounded values within the interval $[0, M[$). It also allows to simulate the variations of light intensity or of camera exposure-time in images.

The aim of this paper is to address both previously listed limitations of the MM application to grey level images by presenting a new framework named *Logarithmic Mathematical Morphology* (LMM) that was recently introduced [18], [19], [20]. Such a framework allows to adjust the amplitude of the structuring function according to the image intensity thanks to the LIP-addition \triangle between the image and the structuring function. LMM extends the theory of MM for images and functions by introducing operations of Logarithmic Image Processing.

In this article and beyond the prior work, the theory of LMM will be detailed. New theoretical results will be added at both following levels. (1) A link will be established between LMM and the functional Asplund metric defined with the LIP-additive law \triangle . Such a metric is robust to lighting variations caused by a change of the light intensity or the camera

exposure-time [17]. (2) New morphological operators with the same robustness to lighting variations will be introduced for non flat structuring functions. LMM will also be validated with experiments and compared to state-of the art methods.

2 RELATED WORK: DETECTION OPERATORS ROBUST TO LIGHTING VARIATIONS

Previously in the literature, there has been some attempts to create operators theoretically robust to lighting changes. However, such operators generally do not take into account the physical causes of these lighting changes such as variations of light intensity or equivalently variations of camera exposure-time. In LMM, these causes are modelled by the LIP-additive law \triangle [17]. Fig.1, shows an image composed of a spiral, a lighting drift and two confounding curves (Fig. 1a). In this example, the LMM operator better detects the spiral without the confounding curves (Fig. 1f) than the usual methods based on a top-hat (Fig. 1d) or a logarithmic top-hat (Fig. 1e).

Let $f : D \rightarrow \overline{\mathbb{R}}$ be a function defined on a domain $D \subset \mathbb{R}^n$ whose values are lying in $\overline{\mathbb{R}} = \mathbb{R} \cup \{-\infty, +\infty\}$. Let $b : D \rightarrow \overline{\mathbb{R}}$ be a structuring function whose values are equal to $-\infty$ outside a domain $D_b \subset D$, $\forall x \in D \setminus D_b, b(x) = -\infty$. In addition, if its values in D_b are equal to zero, the structuring function is called a (flat) structuring element and it is represented by the upper-case letter B .

2.1 Top-hat operators

Meyer [2], [21] created the *top-hat* operator $TH_B(f)$ to detect peaks in a function f . It is equal to the difference between the function and its morphological opening $\gamma_B(f)$ by a flat structuring element B , $TH_B(f) = f - \gamma_B(f)$. The complementary operation for the detection of valleys is the *bottom-hat* $BTH_B(f)$ defined as the difference between a morphological closing $\phi_B(f)$ of the function and the function itself, $BTH_B(f) = \phi_B(f) - f$. Both top-hats are invariant to artificial variations of intensity caused by the addition or the subtraction of any real constant c to a function f , $TH_B(f + c) = TH_B(f)$ and $BTH_B(f + c) = BTH_B(f)$. However, they are not invariant to any lighting variation with a physical cause and modelled by a LIP-addition \triangle or a LIP-subtraction \triangle of a constant to an image $f : D \rightarrow [O, M[$. To address this issue, Jourlin et al. [16], [22] have introduced LIP top-hats where the LIP-difference \triangle replaces the usual difference “-”. Zaharescu [23] proposed variants of LIP top-hats. However, all these top-hats are still defined with a flat structuring element. They constitute a particular case of the extended tops-hats that will be presented in this paper (in section 5.4).

2.2 Morphological gradients

Beucher [24] defined the *morphological gradient* $\varrho_B(f)$ as the difference between the dilation $\delta_B(f)$ and the erosion $\varepsilon_B(f)$ of a function $f : D \rightarrow \mathbb{R}$ by a flat structuring element B , $\varrho_B(f) = \delta_B(f) - \varepsilon_B(f)$. The so-called “morphological gradient” corresponds in fact to the norm of the usual gradient of a function [25]. In order to be the norm of a gradient, it must be defined with a flat structuring element. It is invariant to the addition or subtraction of any real constant c to a function, $\varrho_B(f + c) = \varrho_B(f)$. However, it is not invariant to a lighting variation with a physical cause and modelled by a LIP-addition \triangle or a LIP-subtraction \triangle of a constant to an image. Jourlin [22] addressed this issue by defining a LIP-morphological gradient where the LIP-difference \triangle replaces the usual difference “-”, $\varrho_B^{LIP}(f) = \delta_B(f) \triangle \varepsilon_B(f)$.

2.3 Scale Invariant Feature Transform (SIFT)

Lowe introduced the *Scale Invariant Feature Transform* to detect image features which are “partially invariant to change in illumination” [26]. In SIFT, salient points are first detected as some extrema of a function scale-space obtained by differences between Gaussian filtering of the image. A local image descriptor is then associated to each salient point. This image descriptor is based on an orientation histogram of the gradient of the Gaussian filtered image. As the gradient is computed by differences between image values, this makes it insensitive to illumination changes caused by the addition of a constant. The orientation is weighted by the norm of the gradient which is equal to the so-called “morphological gradient” and has therefore the same invariance. In addition, a normalisation between 0 and 1 of the orientation histograms makes the SIFT descriptor invariant to the multiplication of the image by a constant. However, such invariances do not have any physical causes.

2.4 Trees of connected components

Trees of connected components are based on *level sets*. An image *level set* is the set of these pixels whose values are greater or equal to a given threshold value. By increasing the threshold value, the connected components of a higher level set are included within the connected components of a lower level set. These inclusion relations can be represented by trees of connected components. Various types of trees can be built according to the inclusion relation between the level sets. One can cite e.g., the component-tree, also named max-tree [27], or the tree of shapes, also named inclusion tree [28]. Recent segmentation methods by trees of connected components have been presented in [29], [30]. Trees of connected components of a real function are theoretically invariant to intensity changes caused by applying to the function a continuous and increasing transformation. However, as the intensity of an image is quantised in discrete values in the range $\llbracket 0, 1, \dots, M - 1 \rrbracket$ with a constant step, the lower intensities are poorly represented by these discrete values. For this reason, in low-lighted images, the connected components trees may present a limited robustness to lighting variations [31].

2.5 Intensity variant Mathematical Morphology

Heijmans [6] named *t-operators* the usual morphological operators for functions because of their invariance under horizontal translation (i.e. in space) and under vertical translation (i.e. in intensity). He also defined a class of morphological operators, the *h-operators*, which are invariant under *horizontal* translation but adaptive in the vertical domain (i.e. in intensity). Although the examples of *h-operators* given in [6] were mathematically well-defined for real functions, they were not physically justified. LMM operators form a particular case of *h-operators* which are in addition defined for functions with bounded values such as images and are physically justified.

3 BACKGROUND

3.1 Mathematical Morphology

MM is defined on *complete lattices* [7], [32], [33]. A set \mathcal{L} on which a partial order relation is defined is called a *complete lattice* if every subset \mathcal{X} of \mathcal{L} has an infimum (i.e., a greatest lower bound), $\wedge \mathcal{X}$, and a supremum (i.e., a least upper bound), $\vee \mathcal{X}$. In the case of MM for functions, the set of functions $\overline{\mathbb{R}}^D$ defined on a domain D with values in $\overline{\mathbb{R}}$ is a complete lattice with the order \leq . The infimum and the supremum are defined for any family $\mathcal{X} \subset \overline{\mathbb{R}}^D$ by $(\wedge \mathcal{X})(x) = \wedge_{\overline{\mathbb{R}}} \{f(x) : f \in \mathcal{X}, x \in D\}$ and $(\vee \mathcal{X})(x) = \vee_{\overline{\mathbb{R}}} \{f(x) : f \in \mathcal{X}, x \in D\}$, respectively. The least and greatest elements, O and I , are the constant functions equal to $O(x) = -\infty$ and $I(x) = +\infty$, for all $x \in D$, respectively. Between any two complete lattices \mathcal{L}_1 and \mathcal{L}_2 , the fundamental morphological operations of *erosion* and *dilation* are defined as follows [7], [33], [34].

Definition 1. A mapping or an operator $\varepsilon : \mathcal{L}_1 \rightarrow \mathcal{L}_2$ is an *erosion*, if and only if (iff) it distributes over infima, that is $\varepsilon(\wedge \mathcal{X}) = \wedge \varepsilon(\mathcal{X})$, for any family $\mathcal{X} \subset \mathcal{L}_1$. The operator $\delta : \mathcal{L}_2 \rightarrow \mathcal{L}_1$ is a *dilation*, iff it distributes over suprema, that is $\delta(\vee \mathcal{X}) = \vee \delta(\mathcal{X})$, for any $\mathcal{X} \subset \mathcal{L}_2$.

The definitions of these mappings apply even to the empty subset \emptyset of \mathcal{L}_1 or \mathcal{L}_2 because of the relations $O = \vee \emptyset$ and $I = \wedge \emptyset$ [7]. We have therefore: $\varepsilon(I) = I$ and $\delta(O) = O$. Moreover, the pair (ε, δ) forms an *adjunction* between \mathcal{L}_1 and \mathcal{L}_2 if for all $X \in \mathcal{L}_1, Y \in \mathcal{L}_2$ there is

$$\delta(Y) \leq X \Leftrightarrow Y \leq \varepsilon(X). \quad (1)$$

In an *adjunction* (ε, δ) , ε is an *erosion* and δ a *dilation* [7]. If one reverses the ordering of both lattices \mathcal{L}_1 and \mathcal{L}_2 , the dilation becomes an erosion and vice versa. The erosion and the dilation are called *adjunct operators*. The adjunction constitutes a bijection between the erosion and the dilation. For every dilation δ , there is a unique erosion ε such as (ε, δ) is an adjunction and vice-versa. Moreover, if (ε, δ) is an *adjunction*, then the combination $\delta\varepsilon$ is an *opening* on \mathcal{L}_1 and the combination $\varepsilon\delta$ is a *closing* on \mathcal{L}_2 [35]. *Opening* and *closing* are morphological filters defined as follows [1], [2], [35].

Definition 2. An operator $\psi : \mathcal{L} \rightarrow \mathcal{L}$ on the complete lattice \mathcal{L} is called an *opening* if ψ is increasing ($\forall X, Y \in \mathcal{L}$, if $X \leq Y$ then $\psi(X) \leq \psi(Y)$), anti-extensive ($\forall X \in \mathcal{L}$, $\psi(X) \leq X$) and idempotent ($\psi \circ \psi = \psi$). ψ is a *closing* if it is increasing, extensive ($\forall X \in \mathcal{L}$, $X \leq \psi(X)$) and idempotent.

In the lattice $\overline{\mathbb{R}}^D$ of real functions, let $b : D \rightarrow \overline{\mathbb{R}}$ be a structuring function which is invariant under horizontal and vertical translations. The functional dilation $\delta_b : \overline{\mathbb{R}}^D \rightarrow \overline{\mathbb{R}}^D$ and erosion $\varepsilon_b : \overline{\mathbb{R}}^D \rightarrow \overline{\mathbb{R}}^D$ are *t-operators* which are usually expressed [2] by:

$$\delta_b(f)(x) = \vee \{f(x-h) + b(h), h \in D\} = (f \oplus b)(x) \quad (2)$$

$$\varepsilon_b(f)(x) = \wedge \{f(x+h) - b(h), h \in D\} = (f \ominus b)(x). \quad (3)$$

In the case of ambiguous expressions, the following conventions are used: $f(x-h) + b(h) = -\infty$ when $f(x-h) = -\infty$ or $b(h) = -\infty$, and $f(x+h) - b(h) = +\infty$ when $f(x+h) = +\infty$ or $b(h) = -\infty$ [7]. The symbols \oplus and \ominus represent the extension to functions of Minkowski operations between sets [2]. Overviews of MM are available in [34], [36], [37], [38], [39] and some recent advances in the field can be found in [40], [41], [42], [43].

3.2 Logarithmic Image Processing

The LIP model is a mathematical framework which allows to process images in a way which is compatible with the human visual system [10], [17]. This makes it valid not only for images acquired with transmitted light but also with reflected light. The LIP model is based on the *physical law of transmittances*, $T_{f \triangle g}(x) = T_f(x) \cdot T_g(x)$, where the transmittance $T_{f \triangle g}$ of the superimposition of two semitransparent objects generating the images f and $g \in \mathcal{I} = [0, M]^D$ is equal to the point-wise product of their respective transmittances T_f and T_g . The transmittance $T_f(x)$ at point $x \in D$ is also related to the image grey value $f(x)$ by the equation $T_f(x) = 1 - f(x)/M$, where M is the upper-bound of the grey value interval $[0, M]$. Due to this relation, the LIP-scale is inverted compared to the usual grey scale (Fig. 1b). This means that 0 corresponds to the white extremity, when there is no obstacle between the light source and the camera, whereas M corresponds to the black extremity when no light is passing. By replacing the transmittances T_f and T_g by their expressions in the transmittance law, the addition \triangle of two images f and g is deduced:

$$f \triangle g = f + g - \frac{f \cdot g}{M}. \quad (4)$$

In transmitted light, the addition of two images corresponds to the superimposition of two semitransparent objects generating the images f and g . From (4), the LIP-multiplication \triangle of an image by a scalar $\lambda \in \mathbb{R}$ is deduced, $\lambda \triangle f = M - M(1 - f/M)^\lambda$. It is equivalent to a variation of thickness or opacity of the object by a factor λ . If $\lambda > 1$, the image becomes darker, whereas if $\lambda \in [0, 1]$ it becomes brighter. The opposite function $\triangle f = -1 \triangle f$ is then deduced:

$$\triangle f = \frac{-f}{1 - f/M}. \quad (5)$$

One can notice that $\triangle f$, where $f \geq 0$, is not an image as it takes negative values. It belongs to the set $\mathcal{F}_M =]-\infty, M[^D$ of real functions f whose values are bounded by M , $f : D \rightarrow]-\infty, M[$. From a physical point of view, the negative values $\triangle f$, where $f \geq 0$, are light intensifiers that can be used to compensate the attenuation of the semi-transparent object generating the image f . Their superimposition with the image f is equal to zero (i.e. the white intensity), $f \triangle (\triangle f) = f \triangle f = 0$. This is an important physical property that will be used in this paper. In particular, the LIP-addition of a negative constant will allow to compensate the light attenuation due to a variation of camera exposure-time or of light intensity [17]. From (5), the difference between two functions with bounded values f and $g \in \mathcal{F}_M$ is deduced:

$$f \triangle g = \frac{f - g}{1 - g/M}. \quad (6)$$

$f \triangle g$ is an image iff $f \geq g$. The space of functions whose values are bounded by M , $(\mathcal{F}_M, \triangle, \triangle)$, is a *real vector space* and the space of images, $(\mathcal{I}, \triangle, \triangle)$, represents the *positive cone* of this vector space [16], [17]. \mathcal{F}_M and \mathcal{I} are both ordered by the usual order \leq [16].

4 LOGARITHMIC MATHEMATICAL MORPHOLOGY

4.1 The new framework

LMM is defined in the lattice $\overline{\mathcal{F}}_M = [-\infty, M]^D$ of functions with values in $[-\infty, M]$. The infimum \wedge and the supremum \vee are defined for any family $\mathcal{X} \subset \overline{\mathcal{F}}_M$ by $(\wedge \mathcal{X})(x) = \wedge_{[-\infty, M]} \{f(x) \mid f \in \mathcal{X}, x \in D\}$ and $(\vee \mathcal{X})(x) = \vee_{[-\infty, M]} \{f(x) \mid f \in \mathcal{X}, x \in D\}$ respectively. The least and greatest elements, O and I , are the constant functions equal for all $x \in D$ to $O(x) = -\infty$ and $I(x) = M$, respectively. The LIP-additive law \triangle and the LIP-negative law \triangle will allow to perform morphological transformations that are compatible with the human visual system. LMM is based on the adjunct operators of erosion and dilation which will be introduced as follows. Let $f \in \overline{\mathcal{F}}_M$ be a function and $b \in \overline{\mathcal{F}}_M$ a structuring function. Let $\delta_b^\triangle : \overline{\mathcal{F}}_M \rightarrow \overline{\mathcal{F}}_M$ and $\varepsilon_b^\triangle : \overline{\mathcal{F}}_M \rightarrow \overline{\mathcal{F}}_M$ be both mappings defined by:

$$\delta_b^\triangle(f)(x) = \vee \{f(x-h) \triangle b(h), h \in D\} \quad (7)$$

$$\varepsilon_b^\triangle(f)(x) = \wedge \{f(x+h) \triangle b(h), h \in D\}. \quad (8)$$

In the case of ambiguous expressions, the following conventions will be used: $f(x-h) \triangle b(h) = -\infty$ when $f(x-h) = -\infty$ or $b(h) = -\infty$, and $f(x+h) \triangle b(h) = M$ when $f(x+h) = M$ or $b(h) = -\infty$. The following proposition¹ and definition hold.

Proposition 1. *The pair of mappings $(\varepsilon_b^\triangle, \delta_b^\triangle)$ forms an adjunction, where ε_b^\triangle is an erosion and δ_b^\triangle is a dilation.*

Definition 3. *ε_b^\triangle is called a logarithmic-erosion and δ_b^\triangle a logarithmic-dilation.*

As $(\varepsilon_b^\triangle, \delta_b^\triangle)$ forms an adjunction, an *opening* and a *closing* can be defined by combination of both operators of logarithmic-erosion ε_b^\triangle and logarithmic-dilation δ_b^\triangle (see. section 3.1). The operators γ_b^\triangle and φ_b^\triangle defined by

$$\gamma_b^\triangle = \delta_b^\triangle \varepsilon_b^\triangle, \quad (9)$$

$$\varphi_b^\triangle = \varepsilon_b^\triangle \delta_b^\triangle \quad (10)$$

are an *opening* and a *closing* (by adjunction), respectively.

Definition 4. *γ_b^\triangle is called a logarithmic-opening and φ_b^\triangle a logarithmic-closing.*

Another useful property in MM is that the erosion of a function is equal to the dilation of its *negative function*, and vice versa. Such a property is the duality by *negative function* of both operators and, for LMM, it is established in proposition 2. The *negative function* f^* of f is equal to $f^* = \triangle f$ because we have $(f^*)^* = f$ [8].

Proposition 2. *Let $\bar{b} \in \overline{\mathcal{F}}_M$ be the reflected structuring function of b , where $\forall x \in D, \bar{b}(x) = b(-x)$. The logarithmic-erosion ε_b^\triangle and dilation δ_b^\triangle are dual by their negative functions:*

$$(\delta_b^\triangle(f^*))^* = \varepsilon_b^\triangle(f) \quad \text{and} \quad (\varepsilon_b^\triangle(f^*))^* = \delta_b^\triangle(f). \quad (11)$$

1. The proofs of the propositions 1, 2 and 3 are in the Supplementary Material.

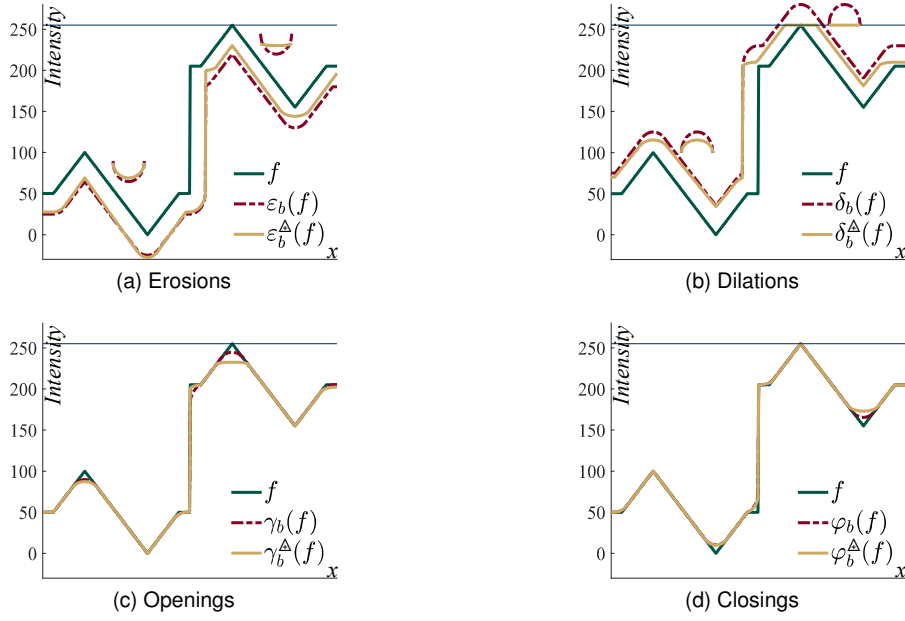


Fig. 2. In an image f (represented in the LIP-scale), comparison between functional MM and LMM for: (a) the erosions $\varepsilon_b(f)$, $\varepsilon_b^\Delta(f)$, (b) the dilations $\delta_b(f)$, $\delta_b^\Delta(f)$, (c) the openings $\gamma_b(f)$, $\gamma_b^\Delta(f)$ and (d) the closings $\varphi_b(f)$, $\varphi_b^\Delta(f)$. (a) and (b) For both image peaks, the structuring function b is represented (after an horizontal translation) for the erosions $\varepsilon_b(f)$, $\varepsilon_b^\Delta(f)$ and the dilations $\delta_b(f)$, $\delta_b^\Delta(f)$.

In the unidimensional image of Fig.2, operators of functional MM are compared to those of LMM. A half-disk serves as structuring function (sf) b . In LMM, the amplitude of the sf changes according to the image values because of the LIP-laws, \triangleleft or \triangle , used in (7) and (8). LMM operators are therefore h -operators which are only invariant under horizontal translation (see section 2.5). However in functional MM, the amplitude of the sf remains the same. This generates t -operators which are invariant under horizontal and vertical translations. Moreover, in Fig.2b, the logarithmic-dilation $\delta_b^\Delta(f)$ of f is always below the upper bound $M = 256$, whereas the functional dilation $\delta_b(f)$ of f may exceed this bound. Such a property is due to the LIP-addition law \triangleleft . In Fig.2a, the negative values of the functional erosion $\varepsilon_b(f)$ have no physical justification, whereas those of the erosion $\varepsilon_b^\Delta(f)$ correspond to light intensifiers. In Fig.2c, the difference between the functional opening $\gamma_b(f)$ and the logarithmic-opening $\gamma_b^\Delta(f)$ is greater for the grey-levels close to M than for those close to zero. Indeed, in LMM, the amplitude of the sf is greater for higher image intensities than for lower intensities because of the non-linearity of the LIP laws \triangleleft and \triangle . The same observation exists between the functional closing $\varphi_b(f)$ and the logarithmic-closing $\varphi_b^\Delta(f)$ (Fig.2d).

4.2 Relation with functional Mathematical Morphology

LMM is defined in the lattice $\overline{\mathcal{F}}_M$, whereas MM for functions is defined in the lattice $\overline{\mathbb{R}}^D$. In order to relate LMM to functional MM, an isomorphism between both lattices is needed. This isomorphism $\xi : \overline{\mathcal{F}}_M \rightarrow \overline{\mathbb{R}}^D$ and its inverse $\xi^{-1} : \overline{\mathbb{R}}^D \rightarrow \overline{\mathcal{F}}_M$ were both defined in [44] by $\xi(f) = -M \ln(1 - f/M)$ and $\xi^{-1}(f) = M(1 - \exp(-f/M))$. With this isomorphism ξ , the following proposition can be established.

Proposition 3. *Let $f \in \overline{\mathcal{F}}_M$ be a function and $b \in \overline{\mathcal{F}}_M$ a structuring function. The logarithmic-dilation δ_b^Δ and the logarithmic-erosion ε_b^Δ are related to the functional dilation δ_b , or $\oplus b$, and erosion ε_b , or $\ominus b$, respectively, by the equations:*

$$\begin{aligned} \delta_b^\Delta(f) &= \xi^{-1}(\delta_{\xi(b)}[\xi(f)]) = \xi^{-1}[\xi(f) \oplus \xi(b)] \\ &= M[1 - \exp(-\delta_b(f))], \end{aligned} \quad (12)$$

$$\begin{aligned} \varepsilon_b^\Delta(f) &= \xi^{-1}(\varepsilon_{\xi(b)}[\xi(f)]) = \xi^{-1}[\xi(f) \ominus \xi(b)] \\ &= M[1 - \exp(-\varepsilon_b(f))], \end{aligned} \quad (13)$$

where $\acute{f} : D \rightarrow \overline{\mathbb{R}}$ is equal to $\acute{f} = -\ln(1 - f/M)$.

These relations facilitate the implementation of the LMM operators as those of usual MM already exist in numerous image analysis software.

4.3 Rank filters

Functional dilations δ_b and erosions ε_b are based on supremum and infimum operations. As supremum and infimum are very sensitive to noise such as speckle [35], they can be replaced by *rank filters* [36] also named *order statistics filters* [45],

percentile filters or rank order filters. The filter of rank k selects the k^{th} smallest element of a set. It corresponds to the k^{th} minimum represented by \wedge^k . Its dual, the k^{th} maximum \vee^k selects the k^{th} greatest element of a set. In (3), a k^{th} minimum filter $\zeta_{b,k} : \mathbb{R} \rightarrow \mathbb{R}$ can be defined by replacing the infimum \wedge by the k^{th} minimum \wedge^k . Similarly, in (2), a k^{th} maximum filter $\vartheta_{b,k}$ can be defined with the k^{th} maximum \vee^k . If $k = 0$, the k^{th} minimum filter $\zeta_{b,0}$ is equal to the functional erosion ε_b and the k^{th} maximum filter $\vartheta_{b,0}$ is equal to the functional dilation δ_b . In LMM, the k^{th} minimum logarithmic filter $\zeta_{b,k}^\Delta : \mathcal{F}_M \rightarrow \mathcal{F}_M$ and the k^{th} maximum logarithmic filter $\vartheta_{b,k}^\Delta$ can also be defined by using the k^{th} minimum \wedge^k and the k^{th} maximum \vee^k in (8) and (7), respectively. The k^{th} minimum and maximum logarithmic filters $\zeta_{b,k}^\Delta$ and $\vartheta_{b,k}^\Delta$ are also related to the k^{th} minimum and maximum filters $\zeta_{b,k}$ and $\vartheta_{b,k}$ by replacing the erosions, ε_b and ε_b^Δ , and dilations, δ_b and δ_b^Δ , by their corresponding rank filters in (13) and (12).

5 OPERATORS ROBUST TO LIGHTING VARIATIONS

Examples of operators robust to lighting changes caused by variations of the camera exposure-time or of the light intensity will be given. These lighting changes are modelled by the LIP-addition of a constant.

5.1 Map of LIP-additive Asplund distances

5.1.1 Link with LMM

The functional Asplund metric with the LIP-additive law Δ was defined by Jourlin [17]. Let f and $g \in \mathcal{F}_M$ be two functions. One of them, e.g. g , is chosen as a probing function and both following numbers are defined: $c_1 = \inf \{c, f \leq c \Delta g\}$ and $c_2 = \sup \{c, c \Delta g \leq f\}$, where c lies within the interval $] -\infty, M[$. c_1 and c_2 are the constants to be LIP-added to the probe b such that it is in contact with the function f from above or from below, respectively. The LIP-additive Asplund metric d_{asp}^Δ is defined by $d_{asp}^\Delta(f, g) = c_1 \Delta c_2$. Importantly, this metric is theoretically invariant under lighting changes modelled by a LIP-addition of a constant: $\forall k \in] -\infty, M[$, $d_{asp}^\Delta(f, g) = d_{asp}^\Delta(f \Delta k, g)$ and $d_{asp}^\Delta(f, f \Delta k) = 0$ [17].

The map of Asplund distances of a function f of \mathcal{F}_M by a probe $b : D_b \rightarrow] -\infty, M[$, where D_b is a subset of D , is the mapping $Asp_b^\Delta : \mathcal{F}_M \rightarrow \mathcal{I}$. Such a mapping is obtained by computing the distance between the function and the probe for each point x of the function domain D . It is defined by $Asp_b^\Delta(f)(x) = d_{asp}^\Delta(f|_{D_b(x)}, b)$, where $f|_{D_b(x)}$ is the restriction of f to the neighbourhood $D_b(x)$ centred on $x \in D$. The map of Asplund distances Asp_b^Δ which was related to MM in [46], [47], [48], is equal to

$$Asp_b^\Delta(f) = c_{1_b}(f) \Delta c_{2_b}(f), \quad (14)$$

where $c_{1_b} : \mathcal{F}_M \rightarrow \mathcal{F}_M$ is the map of the least upper bounds (mlub) and $c_{2_b} : \mathcal{F}_M \rightarrow \mathcal{F}_M$ is the map of the greatest lower bounds (mglb). The mlub c_{1_b} is a dilation and the mglb c_{2_b} is an erosion which are both equal, for all $x \in D$, to:

$$\begin{aligned} c_{1_b}(f)(x) &= \inf_{h \in D_b} \{c, f(x+h) \leq c \Delta b(h)\} \\ &= \vee \{f(x+h) \Delta b(h), h \in D_b\}, \end{aligned} \quad (15)$$

$$\begin{aligned} c_{2_b}(f)(x) &= \sup_{h \in D_b} \{c, c \Delta b(h) \leq f(x+h)\} \\ &= \wedge \{f(x+h) \Delta b(h), h \in D_b\}. \end{aligned} \quad (16)$$

By comparing (15) with (7) and (16) with (8), there exists a strong link between the map of Asplund distances and LMM, as shown in the next proposition².

Proposition 4. Let $f \in \mathcal{F}_M$ be a function and $b \in \mathcal{F}_M$ be a structuring function, where for all $x \in D_b$, $D_b \subset D$, $b(x) > -\infty$. The map of Asplund distances between the function f and the structuring function b is equal to:

$$Asp_b^\Delta(f) = \delta_{\Delta \bar{b}}^\Delta(f) \Delta \varepsilon_b^\Delta(f). \quad (17)$$

For the mlub and the mglb of f , $c_{1_b}(f)$ and $c_{2_b}(f)$, we have:

$$c_{1_b}(f) = \delta_{\Delta \bar{b}}^\Delta(f), \quad (18)$$

$$c_{2_b}(f) = \varepsilon_b^\Delta(f). \quad (19)$$

In the case of ambiguous expressions, the following conventions are used: $Asp_b^\Delta(f)(x) = M$ when $\delta_{\Delta \bar{b}}^\Delta(f)(x) = M$ or $\varepsilon_b^\Delta(f)(x) = -\infty$, and $Asp_b^\Delta(f)(x) = 0$ when $\delta_{\Delta \bar{b}}^\Delta(f)(x) = \varepsilon_b^\Delta(f)(x)$.

As illustrated in Fig.3, the map of Asplund distances consists of a double probing of a function f by the same probe b from above and from below. The mlub $c_{1_b}(f)$ and the mglb $c_{2_b}(f)$ correspond to a dilation $\delta_{\Delta \bar{b}}^\Delta(f)$ and an erosion $\varepsilon_b^\Delta(f)$ of the image f , respectively, by their respective structuring functions $\Delta \bar{b}$ or b (Fig.3b). When the probe b is similar to the image f (according to the Asplund metric), the map of Asplund distances, $Asp_b^\Delta(f)$, of the image presents a minimum. In Fig.3b, both minima of the map of distances correspond to both bumps of the image f (Fig.3a).

2. The proof of proposition 4 is in Supplementary Material.

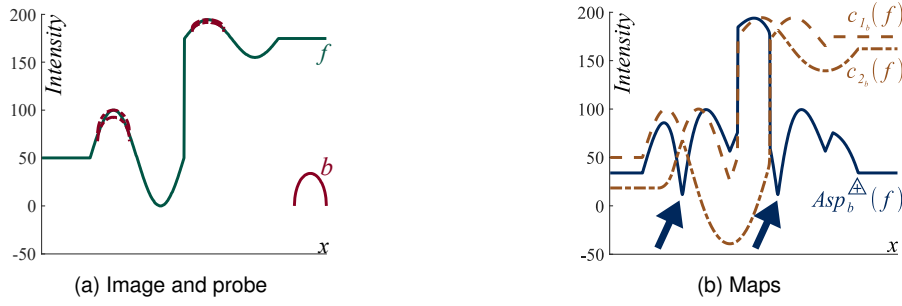


Fig. 3. In the LIP-scale, (a) an image f is analysed by a probe b from above and below. (b) The *mlub* $c_{1_b}(f)$, the *mglb* $c_{2_b}(f)$ and the map of Asplund distances $Asp_b^{\Delta}(f)$ between the image and the probe. Both arrows point towards the minima of the map of Asplund distances.

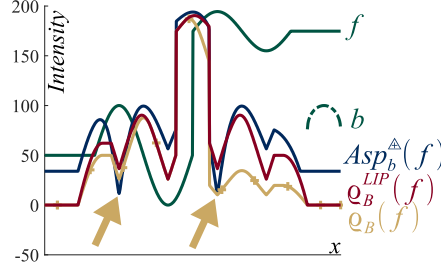


Fig. 4. In the LIP-scale, comparison between the morphological gradient $q_B(f)$, the LIP-morphological gradient $q_B^{LIP}(f)$ and the map of Asplund distances $Asp_b^{\Delta}(f)$ of the image f . The flat structuring element B has the same domain D_B as the one of the structuring function b in Fig.3a. Both arrows point towards the regional minima of the gradients.

5.1.2 Link with the LIP-morphological gradient

Let $b_0 : D \rightarrow \overline{\mathbb{R}}$ be a symmetric and constant structuring element which is defined for all $x \in D_{b_0}$, where $D_{b_0} \subset D$, by $b_0(x) = b_0$ and $b_0(-x) = b_0(x)$. In the case of a symmetric and constant structuring element b_0 , the map of LIP-additive Asplund distances $Asp_{b_0}^{\Delta}$ is equal to the LIP-morphological gradient $q_{B_0}^{LIP}$. For all $x \in D$, we have³:

$$Asp_{b_0}^{\Delta}(f)(x) = q_{B_0}^{LIP}(f)(x). \quad (20)$$

B_0 is a flat structuring element with the same domain D_{b_0} as the one of the constant structuring element b_0 .

When the structuring function b is non flat, the map of LIP-additive Asplund distances Asp_b^{Δ} is an extension of the LIP-morphological gradient q_B^{LIP} . However, contrary to the morphological gradient, the map of Asplund distances is no more the norm of a gradient. For example, let $Y \subset D$ be a constant (i.e., a flat) zone of a function f and let $X = Y \ominus D_b$ be the eroded flat zone by the domain D_b of the structuring function b . \ominus represents the binary erosion [2], [34]. In the eroded flat zone X , the map of Asplund distances is equal to a constant, whereas a gradient and its norm should be equal to zero. We have, for all $x \in X$:

$$Asp_b^{\Delta}(f)(x) = b_{sup} \Delta b_{inf}. \quad (21)$$

b_{sup} and b_{inf} are the supremum and the infimum, respectively, of the structuring function b . In Fig.4, the morphological gradient $q_B(f)$ of the image f and its LIP-morphological gradient $q_B^{LIP}(f)$, both with a flat structuring element B , are compared to the map of Asplund distances $Asp_b^{\Delta}(f)$ with a structuring function b . This structuring function has a bump shape which was designed to detect the bumps of the image f . For both image bumps, the map of Asplund distances $Asp_b^{\Delta}(f)$ presents two deep minima with the same dynamic range, whereas the LIP-morphological gradient $q_B^{LIP}(f)$ and the morphological gradient $q_B(f)$ have two regional minima which have a lower dynamic range. In addition, the regional minima of the morphological gradient $q_B(f)$ have not the same depth between each others. For the flat zones of the image f , both gradients $q_B(f)$ and $q_B^{LIP}(f)$ are equal to zero, whereas the map of Asplund distances $Asp_b^{\Delta}(f)$ is equal to a positive constant defined by (21).

The map of LIP-additive Asplund distances Asp_b^{Δ} is therefore the extension of the LIP-morphological gradient q_B^{LIP} for non flat structuring functions. It gives to this gradient the properties of a metric which is robust to lighting variations. The LIP-morphological gradient is thereby a double probing of an image by a flat structuring element.

5.1.3 Map of Asplund distances with a tolerance to extrema

In the case of discrete images, a map of LIP-additive Asplund distances with a tolerance (to extrema) can be defined as in [47] and related to Mathematical Morphology as follows⁴.

3. The proofs of (20) and (21) are in Supplementary Material.
4. The proof of proposition 5 is in Supplementary Material.

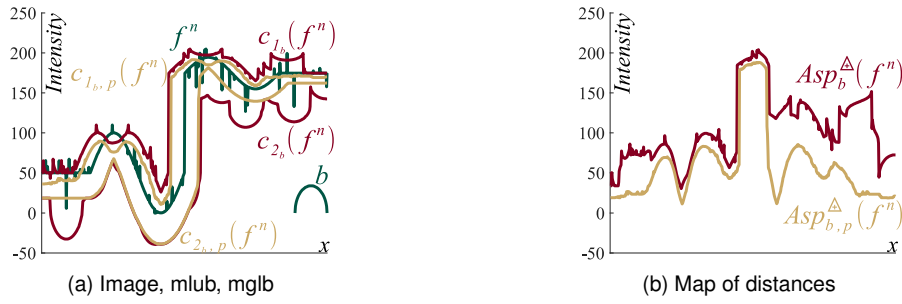


Fig. 5. (a) f^n is an image with a Gaussian white noise, with a standard deviation of 20 grey levels and a density of 0.08. The mlub $c_{1_b}(f^n)$ and the mglb $c_{2_b}(f^n)$ (without tolerance) are compared to the mlub $c_{1_b,p}(f^n)$ and the mglb $c_{2_b,p}(f^n)$ with a tolerance of $p = 85\%$. b is the probe. (b) The map of Asplund distances $Asp_b^\Delta(f^n)$ (without tolerance) is compared to the map of Asplund distances with tolerance $Asp_{b,p}^\Delta(f^n)$. The LIP-scale is used to represent grey-levels.

Proposition 5. Let $f \in \overline{\mathcal{F}}_M$ be a function defined on a discrete grid, e.g. $D \subset \mathbb{Z}^n$. Let $b \in \overline{\mathcal{F}}_M$ be a structuring function, where for all $x \in D_b$, $D_b \subset D$, $b(x) > -\infty$. Let $(1 - p)$ be a percentage of points of D_b to be discarded. The map of LIP-additive Asplund distances with a tolerance p between the function f and the structuring function b is equal to:

$$Asp_{b,p}^\Delta(f) = \vartheta_{\Delta \bar{b}, n_1}^\Delta(f) \triangle \zeta_{b, n_2}^\Delta(f). \quad (22)$$

The number of points to be suppressed, n_1 and n_2 , for the mlub $\vartheta_{\Delta \bar{b}, n_1}^\Delta$ and for the mglb ζ_{b, n_2}^Δ are equal to $n_1 = \text{round}(n_{suppr}/2)$ and $n_2 = n_{suppr} - n_1$, respectively, where $n_{suppr} = \text{round}[(1 - p)\#D_b]$ and $\#D_b$ is the cardinal of D_b . For the mlub, $c_{1_b,p}(f)$, and the mglb of f , $c_{2_b,p}(f)$, we have:

$$c_{1_b,p}(f) = \vartheta_{\Delta \bar{b}, n_1}^\Delta(f), \quad (23)$$

$$c_{2_b,p}(f) = \zeta_{b, n_2}^\Delta(f). \quad (24)$$

In Fig. 5a, a Gaussian white noise is added to the image f of Fig. 3a in order to obtain a noised image f^n . The mlub $c_{1_b}(f^n)$ and the mglb $c_{2_b}(f^n)$ of f^n (without tolerance) are compared to the mlub $c_{1_b,p}(f^n)$ and the mglb $c_{2_b,p}(f^n)$ of f^n with a tolerance p . One can notice that these latter are less sensitive to the local extrema caused by peaks of noise. In Fig. 5b, a similar observation can be made between the map of Asplund distances $Asp_b^\Delta(f^n)$ (without tolerance) and the map of Asplund distances of f^n with tolerance $Asp_{b,p}^\Delta(f^n)$. This latter map has a similar shape as the map of Asplund distances $Asp_b^\Delta(f)$ of the image f without noise (Fig. 3b).

5.2 A novel operator: the LIP-difference between LIP-erosions

In Fig.6, a probe b was designed to detect a bump (Fig.6a) but not a transition (Fig.6b) in a unidimensional image f . The probe b is composed of three elements: (i) the left point b^l , (ii) the right point b^r and (iii) a central bump b^c with approximately the same dynamic range as the bump to be detected but with a smaller width. For each point x of the domain D , the probe is set in contact with the image f from below by LIP-adding a constant c . This latter one is equal to the value of the mglb, $c_{2_b}f(x)$, which has been defined in (16). The LIP-difference is computed between the image f and the left and right points, b^l and b^r , of the probe, $b \triangle c_{2_b}f(x)$, which is in contact with the image f . The left and right detectors, $E(b^l, f)$ and $E(b^r, f) : D \rightarrow]-\infty, M[$, are defined as follows:

$$\begin{aligned} E(b^l, f)(x) &= \wedge_{h \in D_b} \{f(x+h) \triangle [b^l(h) \triangle c_{2_b}(f)(x)]\} \\ &= \wedge_{h \in D_b} \{f(x+h) \triangle b^l(h)\} \triangle c_{2_b}(f)(x), \end{aligned} \quad (25)$$

$$\begin{aligned} E(b^r, f)(x) &= \wedge_{h \in D_b} \{f(x+h) \triangle [b^r(h) \triangle c_{2_b}(f)(x)]\} \\ &= \wedge_{h \in D_b} \{f(x+h) \triangle b^r(h)\} \triangle c_{2_b}(f)(x). \end{aligned} \quad (26)$$

In the event of a bump similar to the probe, the left and right detectors, $E(b^l, f)$ and $E(b^r, f)$, will have close values (Fig. 6a), whereas in the event of a transition, one of the detectors will have a value much higher than the other one (Fig. 6b). Such a property allows to separate bumps (which are similar to the probe) from the transitions. The bump detector $E(b, f) : D \rightarrow]-\infty, M[$ is therefore defined as the point-wise supremum \vee between the left and right detectors:

$$E(b, f) = \vee \{E(b^l, f), E(b^r, f)\}. \quad (27)$$

As illustrated in Fig. 6c, in the event of a bump, the detector presents a deep minimum, whereas in the event of a transition, this minimum disappears. The left and right detectors are related to LMM by the following properties⁵.

5. The proofs of properties 1, 2 and 3 are in Supplementary Material.

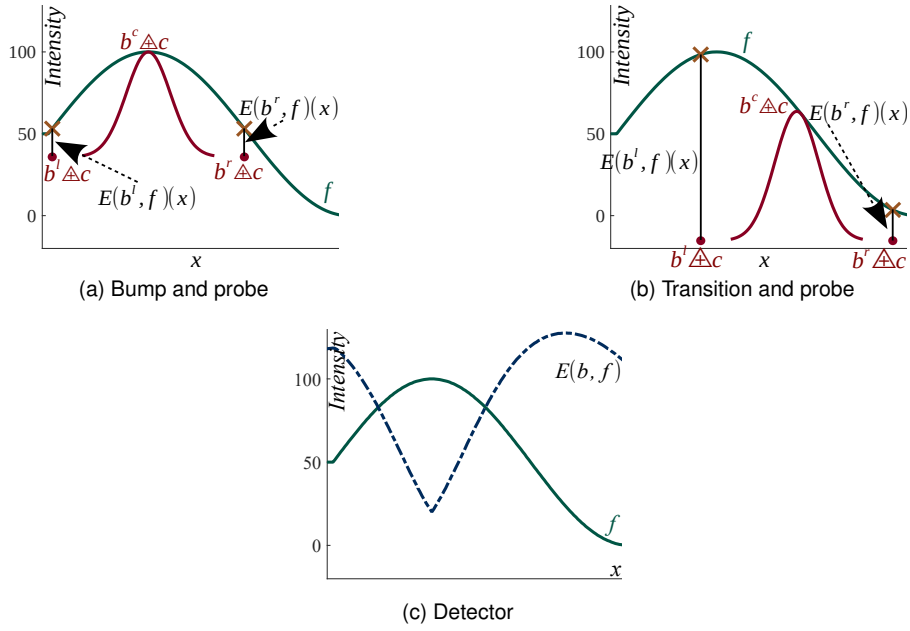


Fig. 6. In the LIP-scale, an image f is analysed by a probe b from below. The objective is to detect (a) a bump but not (b) a transition. After the LIP-addition of a constant c to the probe, $b \triangleleft c$, the left $E(b^l, f)(x)$ and right detectors $E(b^r, f)(x)$ are the LIP-differences between f and the left element b^l of the probe b and its right element b^r , respectively. (c) Bump detector $E(b, f)$.

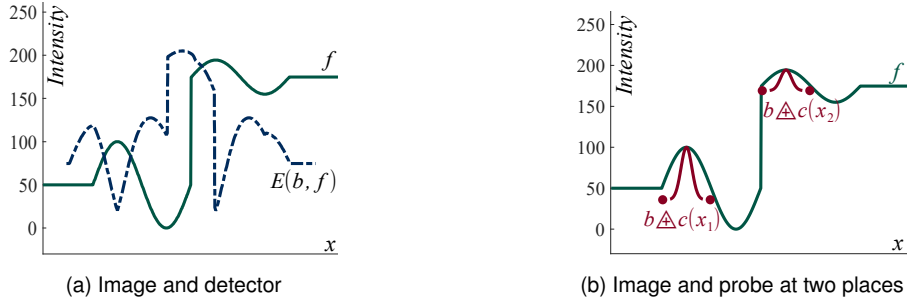


Fig. 7. In the LIP-scale, (a) unidimensional image f and bump detector $E(b, f)$. (b) Image and probe b for two points $x_1, x_2 \in D$.

Property 1. The left and right detectors, $E(b^l, f)$ and $E(b^r, f)$, are equal to LIP-differences between logarithmic-erosions:

$$E(b^l, f) = \varepsilon_{b^l}^{\triangleleft}(f) \triangleleft \varepsilon_b^{\triangleleft}(f), \quad (28)$$

$$E(b^r, f) = \varepsilon_{b^r}^{\triangleleft}(f) \triangleleft \varepsilon_b^{\triangleleft}(f). \quad (29)$$

Property 2. The left and right detectors, $E(b^l, f)$ and $E(b^r, f)$, and the bump detector, $E(b, f)$, are insensitive to the LIP-addition (or the LIP-subtraction) of any constant $c \in]-\infty, M[$ to (or from) the image f :

$$E(b^l, f \triangleleft c) = E(b^l, f),$$

$$E(b^r, f \triangleleft c) = E(b^r, f),$$

$$E(b, f \triangleleft c) = E(b, f).$$

Fig. 7a illustrates the application of the bump detector to a unidimensional image f . The detector presents two minima of the same depth, one for each bump of the image. In the image f , the bump amplitudes are related by the LIP-addition of a constant c which models a change in the image intensity caused by a variation of the light intensity or of the exposure time of the camera. The bump detector $E(b, f)$ is therefore robust to lighting variations modelled by the LIP-addition of a constant. Due to the LIP-addition of the image $mglb, c_{2_b}(f)$, to the probe b , this latter has an amplitude which changes according to the image intensity (Fig. 7b).

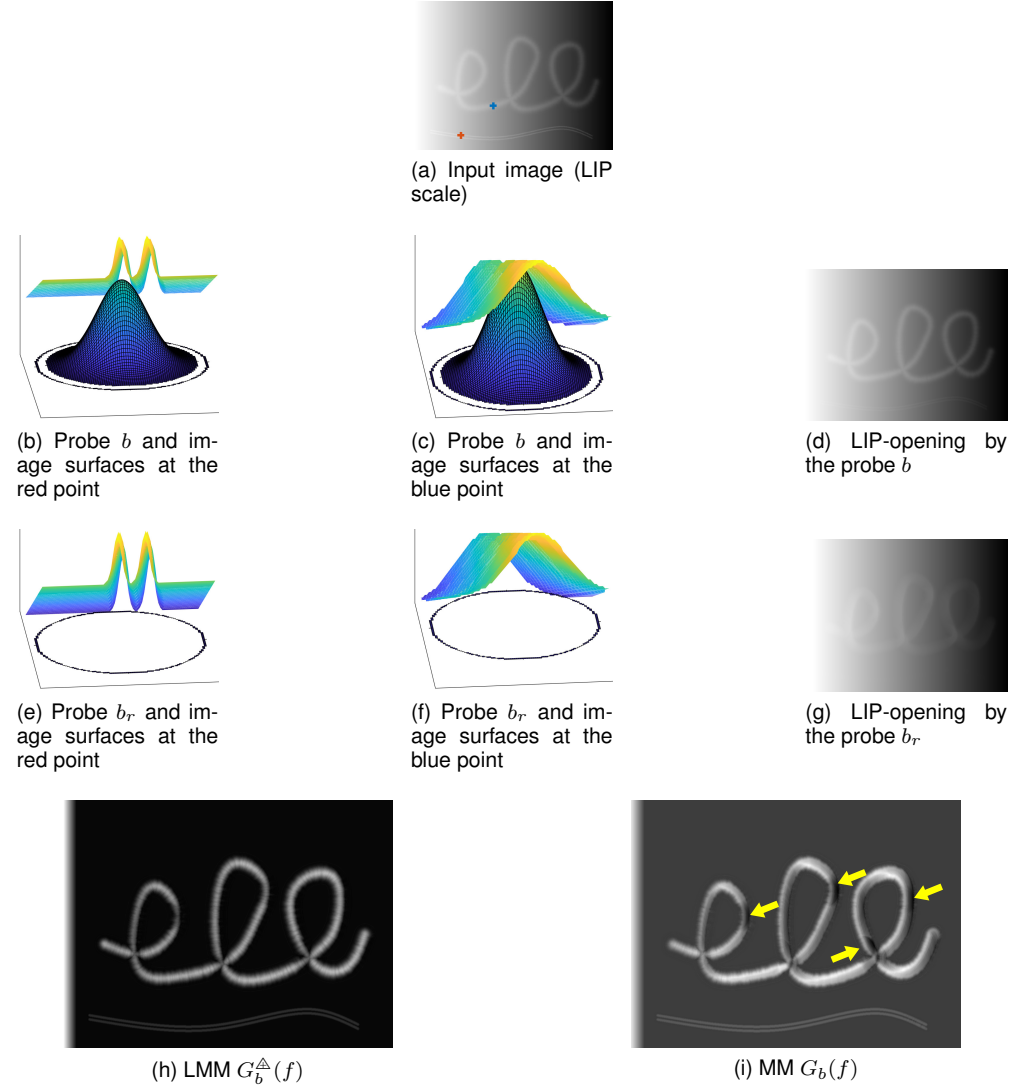


Fig. 8. (a) Selection of two points in the image: the red point is in the curves and the blue point is in the spiral. The image of Fig. 1a is shown in the LIP scale. Intensities of the probe b and the image f represented as a surface: (b) in the curves, for the red point, and (c) in the spiral, for the blue point. (d) LIP-opening $\gamma_b^\Delta(f)$ of the image f by the probe b composed of a Gaussian and a ring. Surfaces of the probe b_r and the image f : (e) in the curves, for the red point, and (f) in the spiral, for the blue point. (g) LIP-opening $\gamma_{b_r}^\Delta(f)$ of the image f by the probe b_r composed of a ring. Results (h) of the LMM operator $G_b^\Delta(f)$ and (i) of the classical MM operator $G_b(f) = \gamma_b(f) - \gamma_{b_r}(f)$. The yellow arrows indicate the contrast changes caused by the lighting drift.

5.3 Other operators: LIP-differences between LIP-morphological operations

In the same way as in section 5.2, the LIP-difference Δ between two operations of LMM can be robust to lighting variations. For example, Fig. 1f illustrates the robustness to a lighting drift, of the operator G_b^Δ defined by:

$$G_b^\Delta(f) = \gamma_b^\Delta(f) \Delta \gamma_{b_r}^\Delta(f). \quad (30)$$

It is equal to the LIP-difference between two logarithmic openings γ_b^Δ and $\gamma_{b_r}^\Delta$ by two different probes b and b_r . b is a Gaussian-shape probe surrounded by a ring (Fig. 1c) and b_r is a ring-shape probe. The operator G^Δ possesses the following property.

Property 3. *The operator $G_b^\Delta : D \rightarrow]-\infty, M[$ is insensitive to the LIP-addition of any constant $c \in]-\infty, M[$ to the function $f : D \rightarrow]-\infty, M[$:*

$$G_b^\Delta(f \Delta c) = G_b^\Delta(f).$$

As the openings are performed by using the probe b defined on a local domain $D_b \subset D$, the operator G_b^Δ is locally (and globally) insensitive to the addition of any constant in this domain D_b . Such a local domain D_b corresponds to a sliding window around any pixel x of the image domain D . In Fig. 1a, the image f presents a lighting drift caused by the LIP-addition of a linear function (i.e. a plane). As a plane (and several other lighting drifts) can be approximated by

a piecewise constant function, the operator G_b^Δ is robust to such a lighting drift. In addition, the Gaussian shape of the probe allows to detect the spiral without detecting both close curves. (i) Firstly, the width of the Gaussian at its top is larger than the width of each one of both curves, but it is smaller than the width of the spiral. When probing the image f , as the probe b is composed of a Gaussian and a ring, it cannot enter into the curves (Fig. 8b), but it can enter into the spiral (Fig. 8c). As a consequence, the logarithmic opening $\gamma_b^\Delta(f)$ of f by the Gaussian and ring probe b almost completely removes both curves but it keeps the spiral (Fig. 8d). (ii) Secondly, the ring probe b_r is larger than the widths of the spiral and of both curves. This prevents it from entering into them (Fig. 8e and 8f). The logarithmic opening $\gamma_{b_r}^\Delta(f)$ of f by the ring b_r strongly attenuates the spiral and removes both curves (Fig. 8g). In the resulting image $G_b^\Delta(f)$ (Fig. 1f or 8h), the LMM operator G_b^Δ extracts the spiral without the lighting drift and strongly attenuates the confounding curves. This image is obtained by the LIP-difference between both openings, $\gamma_b^\Delta(f)$ (Fig. 8d) and $\gamma_{b_r}^\Delta(f)$ (Fig. 8g), of the image f by the probes b and b_r , respectively. However, the classical Mathematical Morphology operator $G_b(f) = \gamma_b(f) - \gamma_{b_r}(f)$ defined as the difference between the openings γ_b and γ_{b_r} (Fig. 8i), does not extract the spiral without keeping contrast changes caused by the lighting drift. A detection robust to lighting drifts – with a physical cause and modelled by the LIP-addition law – is therefore not possible by using classical MM operators, whereas it is possible by using LMM operators.

Other operators robust to lighting variations which are modelled by the LIP-additive law, can be defined as the LIP-difference between LMM operations, e.g.: the LIP-difference between logarithmic-closings or the LIP-difference between an image and its logarithmic-opening (see (32)).

5.4 Extensions of top-hat operators

Let us focus on the difference, or residue, of an image f by its opening $\gamma_b(f)$ or its logarithmic-opening $\gamma_b^\Delta(f)$. Both operators R_b and R_b^Δ are defined as follows:

$$R_b(f) = f - \gamma_b(f), \quad (31)$$

$$R_b^\Delta(f) = f \triangle \gamma_b^\Delta(f). \quad (32)$$

When $b : D \rightarrow]-\infty, M[$ is a flat structuring element denoted by $b = B$, the operators R_b and R_b^Δ correspond to the top-hat operators $TH_B(f) = f - \gamma_B(f)$ and $TH_b^\Delta(f) = f \triangle \gamma_B^\Delta(f)$, respectively. These top-hat operators are presented in section 2.1. When b is a non-flat structuring function, both operators R_b and R_b^Δ constitute extensions of the top-hat operators. The operator R_b is named the *extended top-hat* and the operator R_b^Δ the *extended LIP-top-hat*. However, only this latter operator R_b^Δ possesses the following property⁶.

Property 4. *The extended LIP-top-hat, R_b^Δ , is insensitive to the LIP-addition of any constant $c \in]-\infty, M[$ to the function $f : D \rightarrow]-\infty, M[$: $R_b^\Delta(f \triangle c) = R_b^\Delta(f)$.*

6 EXPERIMENTS AND RESULTS

6.1 Robustness to lighting variations caused by changes in the exposure-time of a camera

6.1.1 Extended top-hats

Let us focus on the extensions of top-hat operators R_b and R_b^Δ defined in section 5.4. Only the extended LIP-top-hat operator R_b^Δ is insensitive to the LIP-addition of any constant c lying in the interval $]-\infty, M[$. As the LIP-addition of a constant models a change of the camera exposure-time or of the source intensity, the logarithmic operator R_b^Δ is expected to have a low sensitivity to such changes. In order to verify this assumption, an experiment has been conducted. An image of the same scene is acquired with two significantly different exposure-times. The scene is composed of a soft toy monster named “Nessie”, which is put down on a white support. (Fig. 9). The first colour image f (Fig. 9a) is captured with a sufficient exposure-time of 1/40s. It is therefore bright and highly-contrasted. Its luminance is denoted by f and it is represented in the LIP-scale: i.e., the inverted greyscale (Fig. 9c). The second colour image f^d (Fig. 9b) is captured with a too small exposure-time of 1/800s, which makes it dark and lowly-contrasted. Its luminance is denoted by f^d (Fig. 9d). The extended top-hat operator R_b is computed on both luminance images f and f^d . The resulting images are denoted by $R_b(f)$ (Fig. 9e) and $R_b(f^d)$ (Fig. 9f). It can be noticed that the extended top-hat in the dark image $R_b(f^d)$ is much less contrasted than in the bright image $R_b(f)$. The extended top-hat operator R_b is therefore sensitive to lighting changes caused by a variation of the camera exposure-time.

The other operator, the extended LIP-top-hat R_b^Δ is then computed on both luminance images f and f^d . The resulting images are denoted by $R_b^\Delta(f)$ (Fig. 9g) and $R_b^\Delta(f^d)$ (Fig. 9h). It can be noticed that both results, $R_b^\Delta(f)$ and $R_b^\Delta(f^d)$, are similar for the most-contrasted part of the scene (i.e, the foreground): the hat, the mouth of “Nessie”, the letters on its body, the bottom of its body and the contour of the white support. For the background (i.e. the very low-contrasted parts of the scene), there exist differences between the results in the bright image $R_b^\Delta(f)$ and in the dark image $R_b^\Delta(f^d)$. They are due to the noise caused by the acquisition in the lowly-contrasted image f^d (Fig. 9b). However, such a noise also exists in the background of the extended top-hat of the dark image $R_b(f^d)$ (Fig. 9f), although it is hidden by some important amplitudes in $R_b(f^d)$. Indeed, when zooming in the background part of $R_b(f^d)$ (Fig. 9f) and rescaling its amplitude, the

6. The proof of property 4 is in Supplementary Material.

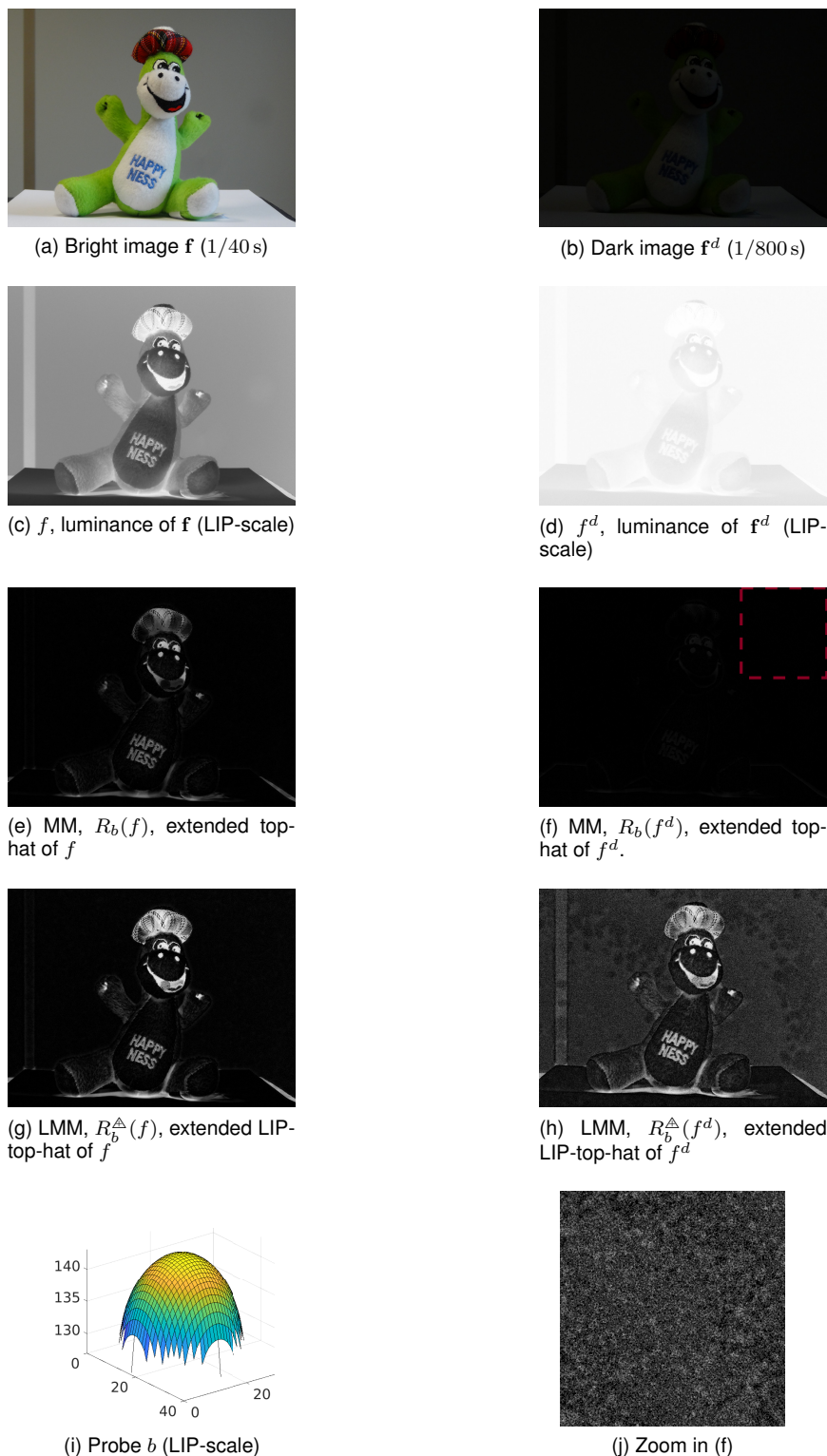


Fig. 9. Comparison of the robustness to camera exposure-times, between the operators of extended top-hat R_b and extended LIP-top-hat R_b^Δ . (a) f and (b) f^d : colour images captured with the camera exposure-times of 1/40 s and 1/800 s, respectively. (c) f and (d) f^d : luminance images (in the LIP-greyscale) of the colour images f and f^d . (e) $R_b(f)$ and (f) $R_b(f^d)$: extended top-hat of f and f^d by the structuring function b . (g) $R_b^\Delta(f)$ and (h) $R_b^\Delta(f^d)$: extended LIP-top-hat of f and f^d by b . (i) The probe b (in the LIP-scale) is made of a 16-pixel radius hemisphere, whose base is set at the grey value 127. (j) Zoom in and rescaling of the background ROI of $R_b(f^d)$, which is in the red rectangle of (f).

noise can be observed (Fig. 9j). It is similar to the one observed in the extended LIP-top-hat of the dark image $R_b^\Delta(f^d)$ (Fig. 9h).

In very low-contrasted parts of a dark image, the extended LIP-top-hat operator R_b^Δ enhances the noise caused by the acquisition; i.e., when very few photons are captured by the camera sensor. However, in the most contrasted parts,

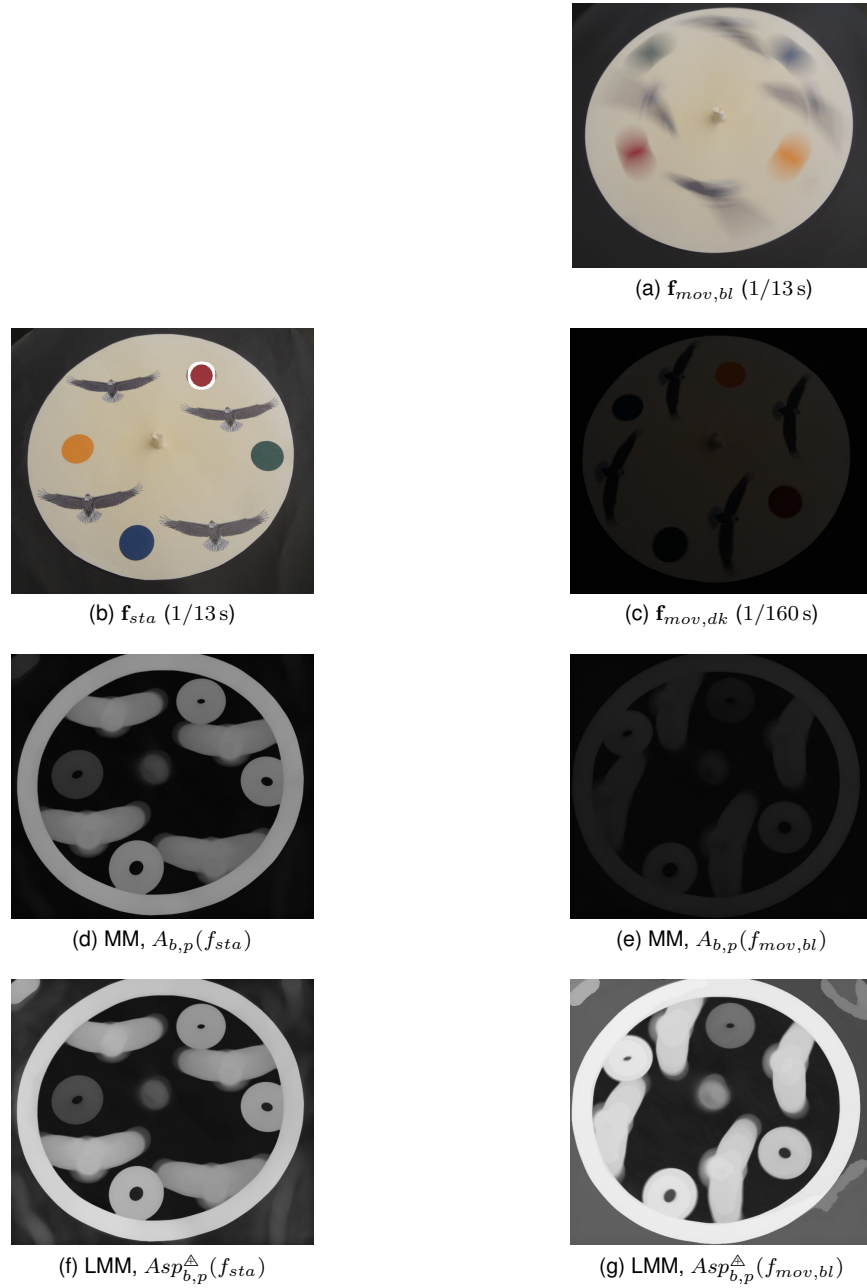


Fig. 10. (a) Colour image $f_{mov,bl}$ of a white disk in rotation and captured with a camera exposure-time of $1/13$ s. (b) Colour image f_{sta} of the same static disk captured with the same camera exposure-time of $1/13$ s. The probe function b is delineated in white. (c) Colour image $f_{mov,dk}$ of the white disk in rotation captured with a camera exposure-time of $1/160$ s. (d) In usual MM, equivalent maps of Asplund distances applied to the luminance of the static disk image, $A_{b,p}(f_{sta})$, and (e) to the luminance of the moving disk image, $A_{b,p}(f_{mov,dk})$. (f) Maps of LIP-additive Asplund distances, with a tolerance p , applied to the luminance of the static disk image, $Asp_{b,p}^{\Delta}(f_{sta})$, and (g) to the luminance of the moving disk image, $Asp_{b,p}^{\Delta}(f_{mov,dk})$. For each map, the tolerance parameter p is set to 95 %.

this extended LIP-top-hat operator R_b^{Δ} has the same amplitude in the bright image $R_b^{\Delta}(f)$ (Fig. 9g) as in the dark image $R_b^{\Delta}(f^d)$ (Fig. 9h). As a consequence, the extended LIP-top-hat operator R_b^{Δ} is much more robust than the extended top-hat operator R_b , to strong lighting variations caused by changes of camera exposure-time.

6.1.2 Map of Asplund distances with a tolerance to extrema

The map of LIP-additive Asplund distances with a tolerance to extrema, $Asp_{b,p}^{\Delta}$, defined in (22), is expected to be robust to strong lighting variations caused by different camera exposure-times. In order to verify this assumption, an experiment is performed with images of a moving object. In those images, the blur effect caused by the movement can be avoided by decreasing the camera exposure-time. However, this is done at the detriment of the image contrast. In Fig. 10, a white disk with patterns is mounted on a turn table of a record player. The patterns include four small coloured disks and confounding shapes (i.e., the eagles). Firstly, in Fig. 10a, an image f_{sta} of the static white disk is captured with an appropriate camera

exposure-time of 1/13 s. This makes the image it well-contrasted. Then, the record player is started up at a speed of 45 revolutions/min. With the same camera exposure-time as the one of f_{sta} , a first image $f_{mov,bl}$ is captured (Fig. 10b). It is correctly contrasted but blurred which makes it useless to detect the coloured disks. In order to suppress the blur effect, the camera exposure-time is decreased to 1/160 s and a second image $f_{mov,dk}$ is captured (Fig. 10c). This second image is not blurred but is darker than the image of the static disk f_{sta} (Fig. 10b). In the luminance images, f_{sta} and $f_{mov,dk}$, of those two differently contrasted images f_{sta} (Fig. 10b) and $f_{mov,dk}$ (Fig. 10c), the map of LIP-additive Asplund distances with a tolerance to extrema $Asp_{b,p}^{\Delta}$ is compared to its equivalent in classical functional MM, $A_{b,p}$, defined as follows:

$$A_{b,p}(f) = \vartheta_{-\bar{b},n_1}(f) - \zeta_{b,n_2}(f). \quad (33)$$

The parameters n_1 and n_2 are defined as in proposition 5. In classical MM, the map $A_{b,p}(f_{sta})$ of the static disk image (Fig. 10d) is brighter than the map $A_{b,p}(f_{mov,dk})$ of the moving disk image (Fig. 10e). However, in LMM, the maps of LIP-additive Asplund distances, with a tolerance, and which are applied to the static disk image $Asp_{b,p}^{\Delta}(f_{sta})$ (Fig. 10f) and to the moving disk image $Asp_{b,p}^{\Delta}(f_{mov,bl})$ (Fig. 10g) are similarly contrasted. Contrary to the maps in classical MM, the LMM maps are therefore robust to strong lighting variations caused by different camera exposure-times.

6.2 Robustness to non-uniform lighting variations in images

In order to test the robustness to non-uniform lighting variations of a segmentation task, a LMM approach [49] is compared to other state-of-the-art methods [50], [51], [52]. The segmentation task consists of extracting vessels in eye fundus images coming from the test set of the DRIVE dataset [53]. However, the testing set is composed of 20 colour eye fundus images which are well contrasted and do not present any significant non-uniform lighting variations. As a consequence, such variations were previously added to those images.

6.2.1 Adding lighting variations to the images

In a colour image $\mathbf{f} = (f_R, f_G, f_B)$, where $\mathbf{f} : D \mapsto [0, M]^3$, the non-uniform lighting variations are generated by LIP-adding a same darkening function $c_{dk} : D \mapsto]-\infty, M[$ to each of the three image components: f_R , f_G and f_B . The darkening function is a 2D increasing function whose origin is located at the centre of the Zone of Interest (ZOI). The ZOI is assimilated to a circle of radius R_o and centre $o = (x_o, y_o)$, where $o \in D \subset \mathbb{R}^2$ (Fig. 11a). Let $\rho \in [0, +\infty[$ and $\theta \in]-\pi, \pi]$ be the polar coordinates of the pixels from the circle centre o . The darkening function c_{dk} is defined by (Fig. 11b):

$$c_{dk}(\rho, \theta) = I_0 \left[1 - \exp\left(\frac{-\rho}{R_o/4}\right) \right].$$

The intensity value $I_0 = 230$ is chosen so that the image is strongly darkened in its external part. The darkened image $\mathbf{f}^{dk} = (f_R^{dk}, f_G^{dk}, f_B^{dk})$ is then defined for each of its components f_i^{dk} as follows:

$$f_i^{dk} = (M - 1) - \lfloor (M - 1 - f_i) \Delta c_{dk} \rfloor,$$

where $\lfloor x \rfloor$ is the floor function of the value $x \in \mathbb{R}^+$. The floor function allows to save the darkened images in png or tif format in order to use them with different segmentation methods. Those darken images have a brighter area in their centre than elsewhere (Fig. 11c).

6.2.2 Vessel segmentation method based on LMM

In [19], [49], a method based on Logarithmic Mathematical Morphology was introduced to segment vessels in eye fundus images. The colour images $\mathbf{f} = (f_R, f_G, f_B)$ are converted to greyscale images in the LIP-scale thanks to the equation $f = M - 1 - (0.299 f_R + 0.587 f_G + 0.114 f_B)$. In this inverted greyscale, the vessels appear as brighter than their surroundings. As in section 5.2, a bump detector is defined. It is based on a 2D probe $b_\theta : D_{b_\theta} \mapsto [0, M[$ composed of 3 parallel segments in the orientation θ and with the same length (Fig. 12a). The probe origin is chosen as one of the extremities of the central segment b_θ^c . Its intensity is greater than the one of the left and right segments b_θ^l and b_θ^r (Fig. 12b). These two segments are equidistant of the central one and the width of the probe is w .

The left and right detectors $E(b_\theta^l, f)$ and $E(b_\theta^r, f)$ of (25) and (26) are now defined with the k^{th} minimum \wedge^k , for any $x \in D$, as follows:

$$\begin{aligned} E^k(b_\theta^l, f)(x) &= \wedge_{h \in D_{b_\theta^l}}^k \{f(x+h) \Delta b_\theta^l(h)\} \Delta \dot{c}_{b_\theta, k}(f)(x) \\ &= \zeta_{b_\theta^l, k}^{\Delta}(f)(x) \Delta \dot{c}_{b_\theta, k}(f)(x) \end{aligned} \quad (34)$$

$$\begin{aligned} E^k(b_\theta^r, f)(x) &= \wedge_{h \in D_{b_\theta^r}}^k \{f(x+h) \Delta b_\theta^r(h)\} \Delta \dot{c}_{b_\theta, k}(f)(x) \\ &= \zeta_{b_\theta^r, k}^{\Delta}(f)(x) \Delta \dot{c}_{b_\theta, k}(f)(x). \end{aligned} \quad (35)$$

The map $\dot{c}_{b_\theta, k}(f)$ is defined as the pointwise infimum \bigwedge of the maps $c_{b_\theta^c}(f)$, $c_{b_\theta^l, k}(f)$ and $c_{b_\theta^r, k}(f)$ for each segment b_θ^c , b_θ^l and b_θ^r of the probe :

$$\begin{aligned} \dot{c}_{b_\theta, k}(f) &= \bigwedge \left\{ c_{b_\theta^c}(f), \bigwedge [c_{b_\theta^l, k}(f), c_{b_\theta^r, k}(f)] \right\} \\ &= \bigwedge \left\{ \varepsilon_{b_\theta^c}^{\Delta}(f), \bigwedge [\zeta_{b_\theta^l, k}^{\Delta}(f), \zeta_{b_\theta^r, k}^{\Delta}(f)] \right\}. \end{aligned}$$

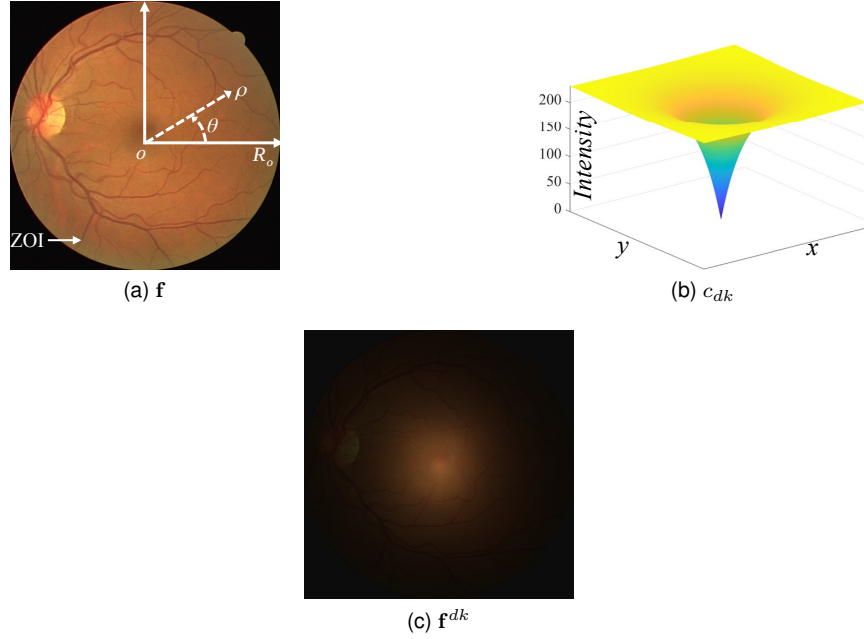


Fig. 11. (a) Colour eye fundus image f , its ZOI and the polar coordinates (ρ, θ) . (b) Surface of the darkening function c_{dk} in the LIP-greyscale. (c) Darkened image f^{dk} .

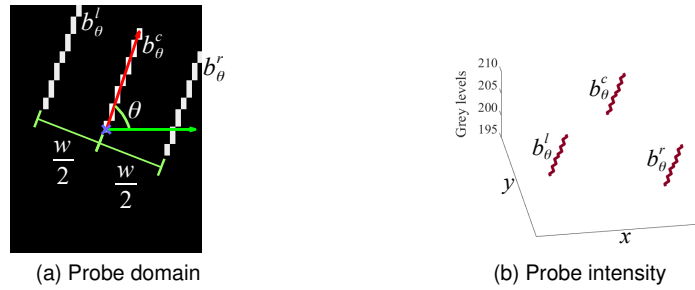


Fig. 12. (a) 2D probe b with an orientation θ and a width w . (b) The central segment b_θ^c has a higher intensity than both others ones b_θ^l and b_θ^r .

As the central segment b_θ^c must fully enter into the vessel relief, the infimum must be extracted and therefore in the previous equation, the map $c_{b_\theta^c}(f) = \wedge \{f(x+h) \triangle b_\theta^c(h), h \in b_\theta^c\} = \varepsilon_{b_\theta^c}^\Delta(f)$ is used (see (16) and (19)). However, in order to reduce the effects of noise for the left and right segments, b_θ^l and b_θ^r , the maps with the k^{th} minimum, $c_{b_\theta^l, k}(f) = \wedge^k \{f(x+h) \triangle b_\theta^l(h), h \in b_\theta^l\} = \zeta_{b_\theta^l, k}^\Delta(f)$ and $c_{b_\theta^r, k}(f) = \zeta_{b_\theta^r, k}^\Delta(f)$, are used (see (24)). As in (27), the bump detector map in orientation θ , $E^k(b_\theta, f)$, is defined by:

$$E^k(b_\theta, f) = \bigvee \{E^k(b_\theta^l, f), E^k(b_\theta^r, f)\}. \quad (36)$$

The bump detector map is expressed as the point-wise infimum of the maps $E^k(b_\theta, f)$ in all the orientations $\theta \in \Theta$:

$$E^k(b, f) = \bigwedge \{E^k(b_\theta, f) \mid \theta \in \Theta\}. \quad (37)$$

As the vessel detection is a multi-scale problem, I different probes, $\{b_i\}_{i \in \llbracket 1 \dots I \rrbracket}$, of width $\{w_i\}_i$ and length $\{l_i\}_i$ will be used. The bump detector maps $E^k(b_i, f)$ for the probes b_i are then combined by point-wise infimum:

$$e_b^k(f) = \bigwedge \{E^k(b_i, f) \mid i \in \llbracket 1 \dots I \rrbracket\}. \quad (38)$$

In the *map of vesselness* $e_b^k(f)$ (Fig. 13a), the vessels appear as valleys. They are extracted by a threshold such that 12% of the ZOI area are considered as vessels (Fig. 13b). $I = 3$ probes with 18 orientations θ between 0° and 360° are chosen. The width w of the probe was chosen in order to be slightly greater than the largest vessel diameter. All the parameters and the experiments used to estimate them are given in [49]. Similarly to property 2, the following property holds⁷.

7. The proof of property 5 is in Supplementary Material

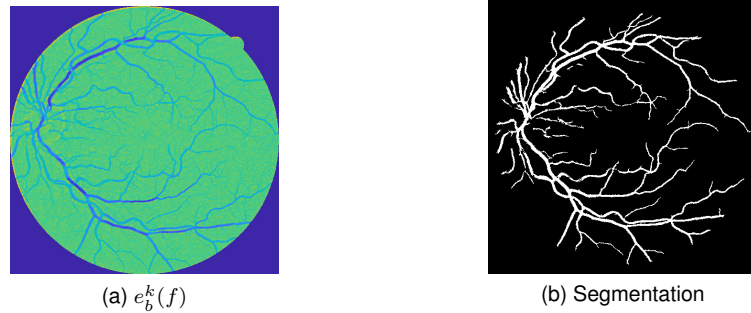


Fig. 13. (a) Map of vesselness $e_b^k(f)$. (b) Vessel segmentation.

TABLE 1

Comparison of the segmentation methods on the test DRIVE dataset with initial and darkened images. Average values over the images are given for the Area Under ROC Curve (AUC), Accuracy (Acc), Sensitivity (Se) and Specificity (Sp). Relative difference (in absolute value) between the AUC for the initial and the dark images (R. Diff).

Method	Images	AUC	Acc	Se	Sp	R. Diff.
LMM	initial	0.9425	0.9624	0.7354	0.9845	2.41 %
	dark	0.9197	0.9547	0.6664	0.9826	
FR-UNet	initial	0.9889	0.9705	0.8356	0.9837	8.48 %
	dark	0.9051	0.9405	0.3683	0.9954	
SGL	initial	0.9882	0.9704	0.8376	0.9834	27.95 %
	dark	0.7120	0.9218	0.1269	0.9982	
RV-GAN	initial	0.9864	0.9650	0.6373	0.9967	31.56 %
	dark	0.6751	0.9124	0.0000	1.0000	

Property 5. The left and right detectors, $E^k(b_\theta^l, f)$ (34) and $E^k(b_\theta^r, f)$ (35), the bump detectors, $E^k(b_\theta, f)$ (36) and $E^k(b, f)$ (37), and the map of vesselness $e_b^k(f)$ (38) are insensitive to the LIP-addition (or the LIP-subtraction) of any constant $c \in]-\infty, M[$ to (or from) an image f :

$$\begin{aligned}
 E^k(b_\theta^l, f \triangle c) &= E^k(b_\theta^l, f), \\
 E^k(b_\theta^r, f \triangle c) &= E^k(b_\theta^r, f), \\
 E^k(b_\theta, f \triangle c) &= E^k(b_\theta, f), \\
 E^k(b, f \triangle c) &= E^k(b, f), \\
 e_b^k(f \triangle c) &= e_b^k(f).
 \end{aligned}$$

The map of vesselness $e_b^k(f)$ is therefore robust to uniform variations of light intensity or of camera exposure-time in an image f . Indeed, such variations are modelled by the LIP-addition (or the LIP-subtraction) of a constant $c \in]-\infty, M[$. The vessel segmentation by this LMM approach is therefore robust to such uniform lighting variations.

6.2.3 Comparison of the LMM approach with other methods

The robustness to non-uniform lighting variations will be tested for the previous approach and state-of-the-art approaches. As explained in section 6.2.1, a non-uniform lighting variation was generated by LIP-adding to the images a function $c_{dk} : D \mapsto]-\infty, M[$ which varies across the domain D , in place of a constant c . The 20 test images of the dataset were darkened.

For comparison purposes, the three best methods of vessel segmentation were selected in the DRIVE dataset using the ranking given in [54]. They are named FR-UNet [50], RV-GAN [51] and SGL (Study Group Learning) [52] and are based on Deep Learning architectures. FR-UNET is based on a multi-resolution U-Net architecture [55]. RV-GAN is composed of a multi-scale Generative Adversarial Network [56]. SGL is based on a U-Net consisting of an image enhancement module and a segmentation module. Those three methods have been tested on the test set using the pre-trained weights given by their authors. In table 1, the performance of each method was evaluated by several indicators for the initial and the darkened images of the test set. The indicators are the mean values over the test set of the Area Under ROC Curve (AUC), Accuracy (Acc), Sensitivity (Se) and Specificity (Sp). Each indicator was computed for each image and the mean value was taken over the test set. The same groundtruth coming from the DRIVE dataset was used. The same program in MATLAB® language was used to estimate those indicators.

The relative difference between the AUC for the initial images and the darkened ones has been computed. The LMM approach obtains the smallest relative difference between AUC with 2.41 %. This is better than the other methods: FR-UNet (8.48 %), SGL (27.95 %) and RV-GAN (31.56 %). In Fig. 14, one can notice that the LMM segmentations are much more

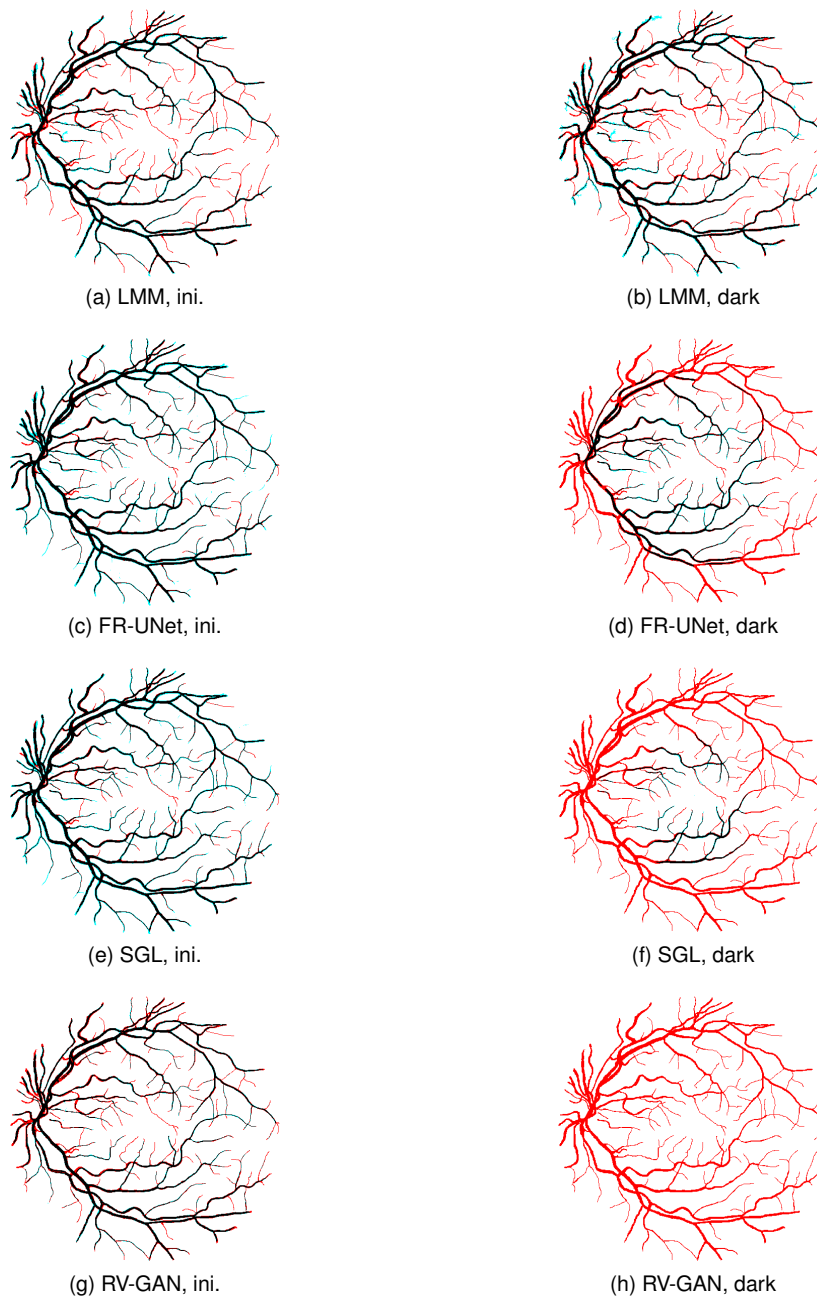


Fig. 14. Segmentation comparison with the groundtruth. Black pixels are true positives, white pixels are true negatives, cyan pixels are false positives and red pixels are false negatives. (a) and (b) LMM segmentations for the initial f and dark f^{dk} images of Fig. 11. (c) and (d) FR-UNet segmentations. (e) and (f) SGL segmentations. (g) and (h) RV-GAN segmentations.

similar between the initial test image (Fig. 14a) and its darkened version (Fig. 14b) than the segmentations with the other approaches. Indeed, in the initial images, the FR-UNet (Fig. 14c), the SGL (Fig. 14e) and the RV-GAN (Fig. 14g) methods obtains good segmentation results. However, in the darkened image, the FR-UNet (Fig. 14d) and the SGL (Fig. 14f) methods only segment the vessels in the brightest part located in the image centre. The RV-GAN approach does not segment the vessels (Fig. 14h).

As a consequence, the LMM approach has a better robustness to non-uniform lighting variations than the other state-of-the-art approaches. This is caused by the LIP-differences between LMM operations (see (34) and (35)) which are used in this approach.

7 CONCLUSION

A new framework named *Logarithmic Mathematical Morphology* (LMM) has been presented. It allows to define Mathematical Morphology operations for images and functions with a upper bound value M by using the Logarithmic Image Processing (LIP) vector space and its additive law \triangle . The sum $f \triangle b$ between two functions f and b with an upper bound value

M is smaller than this upper bound value. The amplitude of the second function, namely the structuring function, varies according to the intensity of the function f and in a way which is physically justified. Such a physical property comes from the LIP model which is defined thanks to the transmittance law and which is coherent with the human vision. The new framework, namely the LMM, allows the definition of morphological operators which are robust to lighting variations modelled by the LIP-additive law \triangle . Those variations correspond to a change of light intensity or of camera exposure-time. Experiments have shown that those operators are robust to such uniform lighting variations and perform better than usual morphological operations defined with the usual additive law $+$. With non-uniform lighting variations, a LMM approach for vessel segmentation in eye-fundus images is more robust than three state-of-the-art methods based on deep-learning, namely FR-UNet, SGL and RVGAN. LMM framework paves the way for the definition of morphological operators and neural nets [20] allowing a robust analysis of images acquired in uncontrolled lighting variations. Such variations occur in numerous practical applications (outdoor scenes, industry, medicine, remote-sensing, etc.)

ACKNOWLEDGMENTS

The author would like to thank Prof. Michel Jourlin for his careful re-reading of the manuscript.

REFERENCES

- [1] G. Matheron, *Random sets and integral geometry*, ser. Wiley ser. in probability and math. statis. New York, NY, USA: Wiley, 1975.
- [2] J. Serra and N. Cressie, *Image Analysis and Mathematical Morphology*. Orlando, FL, USA: Academic, 1982, vol. 1.
- [3] S. R. Sternberg, "Parallel architectures for image processing," in *COMPSAC 79. Proc. Comput. Softw. and The IEEE Comput. Soc.'s Third Int. Appl. Conf.*, Nov. 1979, pp. 712–717.
- [4] S. R. Sternberg, "Grayscale morphology," *Computer Vision, Graphics, and Image Processing*, vol. 35, no. 3, pp. 333 – 355, 1986.
- [5] P. Maragos, "A representation theory for morphological image and signal processing," *IEEE Trans. Pattern Anal. Mach. Intell.*, vol. 11, no. 6, pp. 586–599, Jun. 1989.
- [6] H. J. A. M. Heijmans, "Theoretical aspects of gray-level morphology," *IEEE Trans. Pattern Anal. Mach. Intell.*, vol. 13, no. 6, pp. 568–582, Jun. 1991.
- [7] H. Heijmans and C. Ronse, "The algebraic basis of mathematical morphology I. Dilations and erosions," *Comput. Vision Graphics and Image Process.*, vol. 50, no. 3, pp. 245 – 295, Jun. 1990.
- [8] H. Heijmans, *Morphological image operators*, ser. Adv. Imag. Electron Phys.: Suppl. San Diego, CA, USA: Academic, 1994, no. vol. 25.
- [9] M. Jourlin and J. Pinoli, "A model for logarithmic image-processing," *J. Microsc.*, vol. 149, no. 1, pp. 21–35, Jan. 1988.
- [10] J. Brailean, B. Sullivan, C. Chen, and M. Giger, "Evaluating the EM algorithm for image processing using a human visual fidelity criterion," in *IEEE Int. Conf. Acoustics, Speech, Signal Process.*, Apr. 1991, pp. 2957–2960 vol.4.
- [11] J. Z. Sun, G. I. Wang, V. K. Goyal, and L. R. Varshney, "A framework for bayesian optimality of psychophysical laws," *Journal Math Psychology*, vol. 56, no. 6, pp. 495 – 501, 2012.
- [12] L. R. Varshney and J. Z. Sun, "Why do we perceive logarithmically?" *Significance*, vol. 10, no. 1, pp. 28–31, 2013.
- [13] M. Jourlin, "Chapter One - Gray-Level LIP Model. Notations, Recalls, and First Applications," in *Logarithmic Image Processing: Theory and Applications*, ser. Adv. Imag. Electron Phys., M. Jourlin, Ed. Elsevier, 2016, vol. 195, pp. 1 – 26.
- [14] E. H. Land, "The retinex theory of color vision," *Sci. Am.*, vol. 237, no. 6, pp. 108–129, 1977. [Online]. Available: www.jstor.org/stable/24953876
- [15] R. Kimmel, M. Elad, D. Shaked, R. Keshet, and I. Sobel, "A Variational Framework for Retinex," *Int. J. Comput. Vision*, vol. 52, no. 1, pp. 7–23, Apr. 2003.
- [16] M. Jourlin and J. Pinoli, "Logarithmic image processing: The mathematical and physical framework for the representation and processing of transmitted images," ser. Adv. Imag. Electron Phys. Elsevier, 2001, vol. 115, pp. 129 – 196.
- [17] M. Jourlin, *Logarithmic Image Processing: Theory and Applications*, ser. Adv. Imag. Electron Phys. Elsevier, 2016, vol. 195.
- [18] G. Noyel, "Logarithmic mathematical morphology: A new framework adaptive to illumination changes," ser. Lect. Notes Comput. Sci., vol. 11401. Springer, 2019, pp. 453–461.
- [19] —, "Morphological and logarithmic analysis of large image databases," Dissertation of Accreditation to supervise Research, Université de Reims Champagne-Ardenne, France, Jun. 2021. [Online]. Available: <https://tel.archives-ouvertes.fr/tel-03343079>
- [20] G. Noyel, E. Barbier-Renard, M. Jourlin, and T. Fournel, "Logarithmic morphological neural nets robust to lighting variations," ser. Lect. Notes Comput. Sci. Springer, 2022, pp. 462–474.
- [21] F. Meyer, "Iterative image transformations for an automatic screening of cervical smears." *J. Histochemistry & Cytochemistry*, vol. 27, no. 1, pp. 128–135, 1979.
- [22] M. Jourlin and N. Montard, "A logarithmic version of the top-hat transform in connection with the Asplund distance," *Acta Stereologica*, vol. 16, pp. 201 – 208, 1997.
- [23] E. Zaharescu, "Morphological enhancement of medical images in a logarithmic image environment," in *2007 15th Int. Conf. Digit. Signal Process.*, Jul. 2007, pp. 171–174.
- [24] S. Beucher and F. Meyer, "The morphological approach to segmentation: The watershed transformation," in *Math. Morphology in Image Process.* New York, NY, USA: Marcel Dekker, 1993, pp. 433–481.
- [25] S. Beucher, "Image segmentation and mathematical morphology," Thèse, Ecole Nat. Supérieure Mines Paris, Fr., Jun. 1990. [Online]. Available: <https://pastel.archives-ouvertes.fr/tel-00108290>
- [26] D. G. Lowe, "Distinctive image features from scale-invariant keypoints," *Int. J. Comput. Vision*, vol. 60, no. 2, pp. 91–110, Nov. 2004.
- [27] P. Salembier, A. Oliveras, and L. Garrido, "Antiextensive connected operators for image and sequence processing," *IEEE Trans. Image Process.*, vol. 7, no. 4, pp. 555–570, Apr. 1998.
- [28] P. Monasse and F. Guichard, "Fast computation of a contrast-invariant image representation," *IEEE Trans. Image Process.*, vol. 9, no. 5, pp. 860–872, May 2000.
- [29] N. Passat, B. Naegel, F. Rousseau, M. Koob, and J.-L. Dietemann, "Interactive segmentation based on component-trees," *Pattern Recogn.*, vol. 44, no. 10, pp. 2539 – 2554, 2011.
- [30] Y. Xu, T. Géraud, and L. Najman, "Connected filtering on tree-based shape-spaces," *IEEE Trans. Pattern Anal. Mach. Intell.*, vol. 38, no. 6, pp. 1126–1140, Jun. 2016.
- [31] G. Noyel and M. Jourlin, "Region homogeneity in the logarithmic image processing framework: Application to region growing algorithms," *Image Anal. & Stereology*, vol. 38, no. 1, pp. 43–52, 2019.
- [32] G. Birkhoff, *Lattice Theory*, 3rd ed., ser. Amer. Math. Soc. Colloq. Publications. Providence, RI: AMS, 1967, vol. 25.

- [33] G. J. F. Banon and J. Barrera, "Decomposition of mappings between complete lattices by mathematical morphology, part I: General lattices," *Signal Process.*, vol. 30, no. 3, pp. 299–327, Feb. 1993.
- [34] J. Serra, *Image analysis and mathematical morphology: Theoretical advances*. San Diego, CA, USA: Academic, 1988, vol. 2.
- [35] C. Ronse and H. Heijmans, "The algebraic basis of mathematical morphology: II. Openings and closings," *CVGIP: Image Understanding*, vol. 54, no. 1, pp. 74–97, 1991.
- [36] P. Soille, *Morphological Image Analysis: Principles and Applications*, 2nd ed. New York: Springer-Verlag, 2003.
- [37] L. Najman and H. Talbot, *Mathematical Morphology: From Theory to Applications*, 1st ed. Hoboken, NJ, USA: Wiley, 2013.
- [38] F. Meyer, *Topographical Tools for Filtering and Segmentation 1: Watersheds on Node- or Edge-weighted Graphs*. USA: Wiley, 2019.
- [39] —, *Topographical Tools for Filtering and Segmentation 2: Flooding and Marker-based Segmentation on Node- or Edge-weighted Graphs*. Hoboken, NJ, USA: Wiley, 2019.
- [40] N. Bouaynaya and D. Schonfeld, "Theoretical foundations of spatially-variant mathematical morphology part II: Gray-level images," *IEEE Trans. Pattern Anal. Mach. Intell.*, vol. 30, no. 5, pp. 837–850, May 2008.
- [41] R. Verdú-Monedero, J. Angulo, and J. Serra, "Anisotropic morphological filters with spatially-variant structuring elements based on image-dependent gradient fields," *IEEE Trans. Image Process.*, vol. 20, no. 1, pp. 200–212, Jan. 2011.
- [42] J. J. van de Gronde and J. B. T. M. Roerdink, "Group-invariant colour morphology based on frames," *IEEE Trans. Image Process.*, vol. 23, no. 3, pp. 1276–1288, Mar. 2014.
- [43] O. Merveille, H. Talbot, L. Najman, and N. Passat, "Curvilinear structure analysis by ranking the orientation responses of path operators," *IEEE Trans. Pattern Anal. Mach. Intell.*, vol. 40, no. 2, pp. 304–317, Feb 2018.
- [44] M. Jourlin and J.-C. Pinoli, "Image dynamic range enhancement and stabilization in the context of the logarithmic image processing model," *Signal Process.*, vol. 41, no. 2, pp. 225–237, Jan. 1995.
- [45] P. Maragos and R. Schafer, "Morphological filters—part II: Their relations to median, order-statistic, and stack filters," *IEEE Trans. Acoust., Speech, Signal Process.*, vol. 35, no. 8, pp. 1170–1184, Aug. 1987.
- [46] G. Noyel and M. Jourlin, "Double-sided probing by map of Asplund's distances using logarithmic image processing in the framework of mathematical morphology," ser. Lect. Notes Comput. Sci., vol. 10225. Springer, 2017, pp. 408–420.
- [47] —, "Functional asplund metrics for pattern matching, robust to variable lighting conditions," *Image Analysis & Stereology*, vol. 39, no. 2, pp. 53–71, 2020.
- [48] G. Noyel, "A link between the multiplicative and additive functional asplund's metrics," ser. Lect. Notes Comput. Sci., vol. 11564. Springer, 2019, pp. 41–53.
- [49] G. Noyel, C. Vartin, P. Boyle, and L. Kodjikian, "Retinal vessel segmentation by probing adaptive to lighting variations," in *IEEE 17th Int. Sympo. Biomed. Imag. (ISBI)*, 2020, pp. 1246–1249.
- [50] W. Liu, H. Yang, T. Tian, Z. Cao, X. Pan, W. Xu, Y. Jin, and F. Gao, "Full-resolution network and dual-threshold iteration for retinal vessel and coronary angiograph segmentation," *IEEE J. Biomed. Health Inform.*, vol. 26, no. 9, pp. 4623–4634, 2022.
- [51] S. A. Kamran, K. F. Hossain, A. Tavakkoli, S. L. Zuckerbrod, K. M. Sanders, and S. A. Baker, "RV-GAN: Segmenting retinal vascular structure in fundus photographs using a novel multi-scale generative adversarial network," ser. Lect. Notes Comput. Sci., vol. 12908. Springer, 2021, pp. 34–44.
- [52] Y. Zhou, H. Yu, and H. Shi, "Study group learning: Improving retinal vessel segmentation trained with noisy labels," ser. Lect. Notes Comput. Sci., vol. 12901. Springer, 2021, pp. 57–67.
- [53] J. Staal, M. D. Abramoff, M. Niemeijer, M. A. Viergever, and B. van Ginneken, "Ridge-based vessel segmentation in color images of the retina," *IEEE Trans. Med. Imag.*, vol. 23, no. 4, pp. 501–509, Apr. 2004.
- [54] (2023) Retinal vessel segmentation on DRIVE. [Online]. Available: <https://paperswithcode.com/sota/retinal-vessel-segmentation-on-drive>
- [55] O. Ronneberger, P. Fischer, and T. Brox, "U-net: Convolutional networks for biomedical image segmentation," ser. Lect. Notes Comput. Sci., vol. 9351. Springer, 2015, pp. 234–241.
- [56] I. J. Goodfellow, J. Pouget-Abadie, M. Mirza, B. Xu, D. Warde-Farley, S. Ozair, A. Courville, and Y. Bengio, "Generative adversarial nets," in *NIPS'14*, 2014, p. 2672–2680.